

Benchmarking wave equation solvers using interface conditions: the case of porous media

Haorui Peng¹, Yanadet Sripanich², Ivan Vasconcelos¹ and Jeannot Trampert¹

¹*Department of Earth Sciences, Utrecht University, Utrecht, The Netherlands. E-mail: h.peng@uu.nl*

²*PTT Exploration and Production Public Company Limited, Bangkok, Thailand*

Accepted 2020 September 26. Received 2020 September 16; in original form 2020 May 13

SUMMARY

The correct implementation of the continuity conditions between different media is fundamental for the accuracy of any wave equation solver used in applications from seismic exploration to global seismology. Ideally, we would like to benchmark a code against an analytical Green's function. The latter, however, is rarely available for more complex media. Here, we provide a general framework through which wave equation solvers can be benchmarked by comparing plane wave simulations to transmission/reflection (R/T) coefficients from plane-wave analysis with exact boundary conditions (BCs). We show that this works well for a large range of incidence angles, but requires a lot of computational resources to simulate the plane waves. We further show that the accuracy of a numerical Green's function resulting from a point-source spherical-wave simulation can also be used for benchmarking. The data processing in that case is more involved than for the plane wave simulations and appears to be sufficiently accurate only below critical angles. Our approach applies to any wave equation solver, but we chose the poroelastic wave equation for illustration, mainly due to the difficulty of benchmarking poroelastic solvers, but also due to the growing interest in imaging in poroelastic media. Although we only use 2-D examples, our exact R/T approach can be extended to 3-D and various cases with different interface configurations in arbitrarily complex media, incorporating, for example, anisotropy, viscoelasticity, double porosities, partial saturation, two-phase fluids, the Biot/squirt flow and so on.

Key words: Permeability and porosity; Numerical modelling; Wave propagation.

1 INTRODUCTION

As seismic waves travel through a medium, information about the internal properties of the medium is collected along their paths. Many methods are developed to extract this information directly from the waves recorded, aiming to reconstruct a model of the medium's interior. State-of-the-art examples are full waveform inversion (FWI) methods (Virieux & Operto 2009). In industry, the use of seismic amplitudes as a function of incidence angle or offset (AVO), is often used to infer details of subsurface properties, such as quantitative reservoir characterization or monitoring. Recent years have seen the rise of wave-equation-based (WEB) AVO inversions—a hybrid method combining amplitude-based inversion with the FWI framework. WEB AVO (Haffinger *et al.* 2018) solves a full wave equation to directly invert for medium parameters, for example the compressibility and shear compliance, which can in turn be used to estimate properties such as porosity or fluid content by Gassmann's approximation. Promising as these methods are, it is important to note that the accurate simulation of wave propagation in heterogeneous media is still a challenging task, especially in the case of a complicated geometry with coupled interfaces between different media.

Traditionally, the accuracy of a wave equation solver is checked by relying on an analytical Green's function for special cases (e.g. homogeneous or two-layer models) for benchmarking. However, this approach cannot be applied to more complex media where a closed-form solution to the wave equation is not available. This is often the case for solvers including low-symmetry anisotropy, visco- or poroelastic effects. In porous media, analytical Green's functions for the open-pore acoustic/poroelastic interface and poroelastic/poroelastic interface for 2-D and 3-D cases with zero viscosity have been derived by Diaz & Ezziani (2008a,b,c, 2009). For these two specific interface cases, spectral element benchmarks are already given in Morency & Tromp (2008). However, the analytical Green's function for the open-pore elastic/poroelastic interface is still not available, despite being useful for many applications. For completeness of our

study in porous media, we further examine this case in Appendix A by exploiting the existing poroelastic/poroelastic analytical Green's function.

To address the issue of lacking analytical Green's functions, we propose a simple and flexible framework based on reflection and transmission (R/T) coefficients using the exact boundary conditions (BC) of the problem. Using plane-wave analysis, we show that single-frequency R/T coefficients for waves at specific incidence angles can directly be obtained from the interface conditions, which in turn are controlled by the model parameters on both sides of the interface. Our approach is to compare the R/T coefficients of different waves obtained from plane-wave analysis against those from plane-wave simulations. Point-source simulations, that is the numerical Green's functions, can also be used as they represent an integral over both a continuous range of plane-wave R/T coefficients along the interface and the limited bandwidth of the source wavelet (Ursenbach *et al.* 2007).

We chose to use a poroelastic wave equation to illustrate our approach. Wave propagation in porous media is essential in many geophysical problems such as seismic exploration and CO₂ sequestration (Lumley 2010). Using acoustic or elastic theory with Gassmann's formulae, Morency *et al.* (2011) highlighted observable poroelastic signatures that cannot be captured by comparing acoustic, elastic and poroelastic wave simulations. These differences are significant and need to be considered in a detailed study of reservoir characterization.

It is difficult to obtain a closed-form analytical solutions for general numerical benchmarking. For piecewise homogeneous media, the wave equation must be supplemented with interface conditions that relate the field variables on both sides of the discontinuous surface (Gurevich & Schoenberg 1999). Interface conditions between two poroelastic layers (including also acoustic/poroelastic and elastic/poroelastic) were first derived by Deresiewicz & Skalak (1963) using the uniqueness theorem—whose results are extensively used in poroelasticity studies (e.g. Feng & Johnson 1983; Wu *et al.* 1990; Yang 1999; Denneman *et al.* 2002; Morency & Tromp 2008; Vashisth & Sharma 2009). In terms of validation, Rasolofosaon (1988) and Gurevich (1996) presented laboratory results in support of some of these expressions. Alternatively, Gurevich & Schoenberg (1999) showed that the interface conditions of Deresiewicz & Skalak (1963) can also be derived using a different approach. A more recent discussion on the theoretical derivation of interface conditions involving porous media is presented by Quiroga-Goode (2005).

When it comes to numerically modelling of waves in poroelastic media, various methods have been proposed based on finite difference methods (FD, e.g. Dai *et al.* 1995; Masson *et al.* 2006; Masson & Pride 2007; Wenzlau & Müller 2009; Masson & Pride 2010; Zhang & Gao 2014). To overcome model sampling difficulties encountered in FD approaches, other methods have been proposed, such as the discontinuous Galerkin method (DG), for example de la Puente *et al.* (2008); Dupuy *et al.* (2011) and the spectral element method (SEM), for example Morency & Tromp (2008), the latter becoming an increasingly popular choice for geophysical applications. A detailed review of various techniques and a discussion on numerical implementation aspects related to poroelastic modelling can be found in Carcione *et al.* (2010).

Our approach relies on plane-wave decomposition and/or analysis of the wave data. The geophysical literature counts many studies on plane-wave analysis. Specifically for porous media, plane-wave analysis has been used to study the seismic reflection and transmission of an acoustic/poroelastic interface (e.g. Stoll & Kan 1981; Feng & Johnson 1983; Wu *et al.* 1990), an elastic/poroelastic interface (e.g. Vashisth *et al.* 1991; Sharma & Gogna 1992; Yang 1999) and a poroelastic/poroelastic interface (e.g. Dutta & Odé 1983; Santos *et al.* 1992; Albert 1993; Quiroga-Goode 2005; Yeh *et al.* 2010; Corredor *et al.* 2014).

We first derive expressions for the R/T coefficients for different interface conditions in porous media using plane-wave analysis. With spectral element simulations, we then benchmark four different R/T coefficients—for the reflected P and S wave, the transmitted fast P and the transmitted S wave—in the presence of an elastic/poroelastic interface comparing coefficients obtained from plane-wave simulations against those from plane-wave analysis. Our study shows that even for post-critical angles, the results are in very good agreement. Finally, using point source simulations instead, as the authors explored in preliminary work (Peng *et al.* 2018), we derive the reflection coefficients in the presence of different interfaces and show that this is adequate below critical angles. In all simulations, we used SPECFEM2D 7.0.0, (Tromp *et al.* 2008; Komatitsch *et al.* 2012) published under the CeCILL v2 license.

2 WAVE EQUATIONS, INTERFACE CONDITIONS AND ATTENUATION

2.1 General approach to benchmarking wave equation solvers with interface conditions

Although we focus our benchmarking examples on poroelasticity, we reiterate that our approach based on plane-wave analysis is applicable to any wave equation solver. The method can be summarized as follows:

- (i) Choose a desired wave equation (e.g. viscoelastic, poroelastic, etc.) and a corresponding numerical solver.
- (ii) Set up the interface conditions: these are specific to the wave equation and the interfaces in the media.
- (iii) Use the interface conditions to calculate the exact R/T coefficients through plane-wave analysis.
- (iv) Benchmark the numerical simulations, either by: (i) comparing the results of numerical plane-wave simulations with the exact frequency-dependent R/T coefficients, or (ii) comparing explosive point-source simulations against the R/T coefficients.

Following these steps, we show below several examples of benchmarks in Section 3 and Section 4. Alternatively, the numerical simulations can be benchmarked against analytical Greens's functions if they are available.

2.2 Poroelastic wave equations

The constitutive relation for a 2-D isotropic fluid-saturated homogeneous poroelastic medium is given below (Biot 1956)

$$\begin{cases} \sigma_{xx} = P \frac{\partial u_x}{\partial x} + (P - 2N) \frac{\partial u_z}{\partial z} + Q \left(\frac{\partial U_x}{\partial x} + \frac{\partial U_z}{\partial z} \right) \\ \sigma_{zz} = P \frac{\partial u_z}{\partial z} + (P - 2N) \frac{\partial u_x}{\partial x} + Q \left(\frac{\partial U_x}{\partial x} + \frac{\partial U_z}{\partial z} \right) \\ \sigma_{xz} = N \left(\frac{\partial u_z}{\partial x} + \frac{\partial u_x}{\partial z} \right) \\ p = -\frac{1}{\phi} \left[Q \left(\frac{\partial u_x}{\partial x} + \frac{\partial u_x}{\partial x} \right) + R \left(\frac{\partial U_x}{\partial x} + \frac{\partial U_x}{\partial x} \right) \right], \end{cases} \quad (1)$$

where σ_{xx} , σ_{zz} , σ_{xz} are the normal and shear stresses. u_x , u_z are the x and z components of the displacement vector in the solid frame. U_x , U_z are those in the fluid part. p and ϕ stand for pore pressure and porosity, respectively. The equations of motion for displacement in such a medium can be written as (Biot 1956)

$$\begin{cases} \nabla((P - N)\nabla \cdot \mathbf{u} + Q\nabla \cdot \mathbf{U}) + N\nabla^2 \mathbf{u} = \frac{\partial^2}{\partial t^2}(\rho_{11}\mathbf{u} + \rho_{12}\mathbf{U}) + b_0 \frac{\partial}{\partial t}(\mathbf{u} - \mathbf{U}) \\ \nabla(Q\nabla \cdot \mathbf{u} + R\nabla \cdot \mathbf{U}) = \frac{\partial^2}{\partial t^2}(\rho_{12}\mathbf{u} + \rho_{22}\mathbf{U}) - b_0 \frac{\partial}{\partial t}(\mathbf{u} - \mathbf{U}), \end{cases} \quad (2)$$

where P , Q , R , b_0 are derived as (Feng & Johnson 1983):

$$\begin{cases} P = \frac{(1 - \phi)(1 - \phi - \kappa_{fr}/\kappa_s)\kappa_s + \phi(\kappa_s/\kappa_f)\kappa_{fr}}{1 - \phi - \kappa_{fr}/\kappa_s + \phi\kappa_s/\kappa_f} + \frac{4N}{3} \\ Q = \frac{(1 - \phi - \kappa_{fr}/\kappa_s)\phi\kappa_s}{1 - \phi - \kappa_{fr}/\kappa_s + \phi\kappa_s/\kappa_f} \\ R = \frac{\phi^2\kappa_s}{1 - \phi - \kappa_{fr}/\kappa_s + \phi\kappa_s/\kappa_f} \\ b_0 = \eta\phi^2/k, \end{cases} \quad (3)$$

where N is the shear modulus of both the drained porous solid and the composite. We use \mathbf{u} to denote the displacement vector in the solid frame and \mathbf{U} in the fluid part. k stands for permeability and η for the fluid viscosity. κ_s , κ_f , κ_{fr} represent the bulk moduli of the solid, the fluid and the frame, respectively. ρ_{11} and ρ_{22} denote the effective mass densities of the solid and fluid. ρ_{12} represents the mass coupling effect between the fluid and the solid. They are linked to the density of the solid ρ_s , the fluid ρ_f and tortuosity c by (Molotkov 2002)

$$\begin{cases} \rho_{11} = (1 - \phi)\rho_s - \rho_{12} \\ \rho_{22} = \phi\rho_f - \rho_{12} \\ \rho_{12} = (1 - c)\phi\rho_f. \end{cases} \quad (4)$$

The parameter b_0 defined in eq. (2) makes the viscous resistance to fluid flow frequency-dependent. In poroelasticity, there is a characteristic frequency f_c that separates the low-frequency and high-frequency regimes, given by (Biot 1956)

$$f_c = \frac{\eta\phi}{2\pi c\rho_f k} = \frac{b_0}{2\pi c\rho_f\phi}. \quad (5)$$

At frequencies lower than f_c , the fluid flow is laminar (also known as Poiseuille flow), meaning that inertial forces are negligible compared to viscous forces, which control the flow regime. At frequencies higher than f_c , the fluid velocity distribution within the pores is more complex, and the effects of viscosity are felt only in a thin boundary layer (Morency & Tromp 2008). In this paper, all the simulations are within the low-frequency regime. We have chosen this particular form of Biot's equations out of simplicity for the plane-wave analysis. Another mathematically equivalent form (eq. B1 in Appendix B) according to Biot (1962), which uses the relative displacement of the fluid to the solid is also a valid option. The poroelastic module in SPECFEM2D that we later use for the numerical examples is based on this set of equations (Morency & Tromp 2008). The same set of equations is also used by Yang (1999) for plane-wave analysis.

2.3 Different interface conditions in porous media

We summarize the boundary conditions of the acoustic/poroelastic, the elastic/poroelastic, and the poroelastic/poroelastic interfaces in Table 1 (Deresiewicz & Skalak 1963). We observe that the number of equations for the interface conditions varies from 4 to 6, which can be combined with the corresponding constitutive relations for the three cases (eqs 7, C2 and C4) to yield the R/T coefficients for any chosen wave. Here, we present the equations for the poroelastic/poroelastic interface, while the other two cases are given in Appendix C.

We consider 2-D horizontally layered media in Cartesian geometry (Fig. 1). Therefore, the interface conditions from Table 1 translate

Table 1. Review of different interface conditions involving porous media. Instead of giving the explicit equations, we simply state the boundary conditions.

Interface condition in porous media	
Poroelastic/poroelastic (eq. 6)	Continuity of normal stress Continuity of shear stress Continuity of pore pressure Continuity of vertical velocity in solid part Continuity of horizontal velocity in solid part Continuity of vertical fluid velocity relative to the frame
Elastic/poroelastic (eq C1)	Continuity of normal stress Continuity of shear stress Continuity of vertical velocity in solid part and elastic media Continuity of horizontal velocity in solid part and elastic media Continuity of vertical velocity in solid and fluid parts in poroelastic media
Acoustic/poroelastic (eq. C3)	Continuity of normal stress and pore pressure (poroelastic) Vanishing shear stress (acoustic half-space) Equality of pressure (acoustic) Conservation of fluid volume

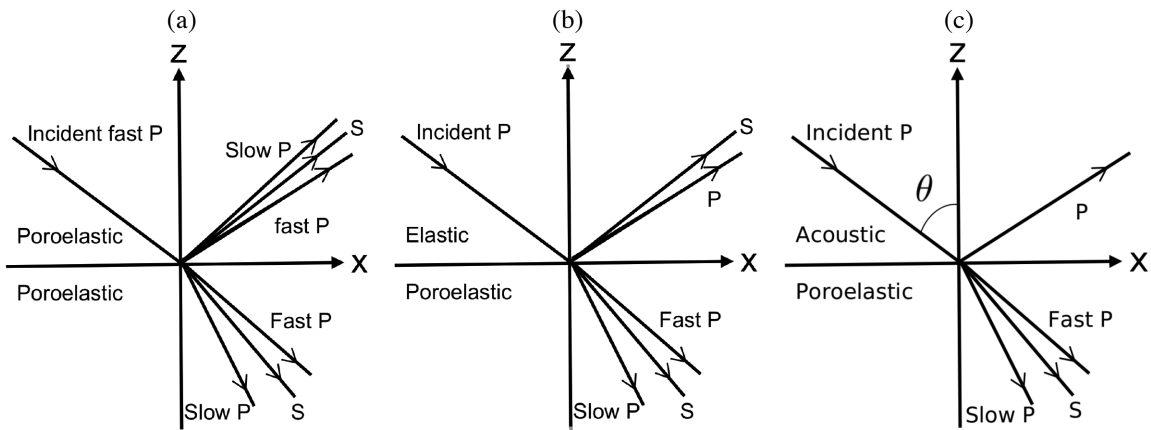


Figure 1. Illustration of the reflection and transmission of an incident (fast) P wave at the poroelastic/poroelastic interface (a), the elastic/poroelastic interface (b) and the acoustic/poroelastic interface (c), respectively.

into

$$\left\{ \begin{array}{l} \sigma_{zz}^t - \phi^t p^t = \sigma_{zz}^b - \phi^b p^b \\ \sigma_{xz}^t = \sigma_{xz}^b \\ p^t = p^b \\ \dot{u}_z^t = \dot{u}_z^b \\ \dot{u}_x^t = \dot{u}_x^b \\ \dot{w}_z^t = \dot{w}_z^b \end{array} \right. \quad (6)$$

Introducing the corresponding constitutive relations (eq. 1), we find

$$\left\{ \begin{array}{l} (P^t - 2N^t + Q^t) \frac{\partial u_x^t}{\partial x} + (P^t + Q^t) \frac{\partial u_z^t}{\partial z} \\ \quad + (Q^t + R^t)(\nabla \cdot \mathbf{U}^t) = (P^b - 2N^b + Q^b) \frac{\partial u_x^b}{\partial x} \\ + (P^b + Q^b) \frac{\partial u_z^b}{\partial z} + (Q^b + R^b)(\nabla \cdot \mathbf{U}^b) \\ N^t \left(\frac{\partial u_z^t}{\partial x} + \frac{\partial u_x^t}{\partial z} \right) = N^b \left(\frac{\partial u_z^b}{\partial x} + \frac{\partial u_x^b}{\partial z} \right) \\ (Q^t (\nabla \cdot \mathbf{u}^t) + R^t (\nabla \cdot \mathbf{U}^t)) / \phi^t = (Q^b (\nabla \cdot \mathbf{u}^b) + R^b (\nabla \cdot \mathbf{U}^b)) / \phi^b \\ \dot{u}_x^t = \dot{u}_x^b \\ \dot{u}_z^t = \dot{u}_z^b \\ \phi^t (\dot{U}_z^t - \dot{u}_z^t) = \phi^b (\dot{U}_z^b - \dot{u}_z^b). \end{array} \right. \quad (7)$$

Note that the subscripts x and z indicate the components of vectors perpendicular and parallel to the interface, respectively. t and b refer to the top and the bottom half-space, separately. $\dot{u}_z, \dot{u}_x, \dot{U}_z$ are velocity fields in the solid frame and the velocity in the fluid part, respectively. \dot{w}_z is the relative velocity of the fluid to the solid frame defined as $\dot{w}_z = \phi(\dot{U}_z - \dot{u}_z)$. According to Deresiewicz & Skalak (1963), the pressure drop across the interface requires

$$p^t - p^b = T\dot{w}_z^t = T\dot{w}_z^b, \quad (8)$$

where T is a coefficient of resistance. The open-pore condition corresponds to $T = 0$ and closed-pore condition $T = \infty$ (i.e. $\dot{w}_z = 0$ and p^t, p^b are not related). $0 < T < \infty$ represents partially open interface. Gurevich & Schoenberg (1999) prove that only the open-pore interface conditions are fully consistent with Biot's equations at the interface. They further state that 'a partially open or impermeable interface may be looked upon as a limiting case of a thin layer with small permeability proportional to the layer thickness, where the open-pore conditions do apply on both sides of this thin layer'. Therefore here we only consider the open-pore case.

2.4 Plane-wave analysis for interface conditions in coupled porous media

Figs 1(a)–(c) illustrate reflection and transmission of an incident (fast) P wave at poroelastic/poroelastic, elastic/poroelastic and acoustic/poroelastic interfaces, respectively. Following Wu *et al.* (1990) and Albert (1993), we derive the plane-wave analysis for the above three interface conditions. A similar approach is also used to study seismic reflection and transmission coefficients of a single layer sandwiched between two dissimilar poroelastic solids (Kumari *et al.* 2017). Starting with the poroelastic/poroelastic interface, we first introduce the scalar potentials ϕ_+, ϕ_- of the fast and the slow P wave, respectively and the vector potential Ψ of the S wave in the poroelastic half-space.

$$\begin{cases} \mathbf{u} = \nabla\phi_+ + \nabla\phi_- + \nabla \times \Psi \\ \mathbf{U} = -\varrho_+ \nabla\phi_+ - \varrho_- \nabla\phi_- + \varrho_{sh} \nabla \times \Psi \end{cases} \quad (9)$$

with $\Psi = [0, \psi, 0]$. Following Stein & Wysession (2003), the vector potential Ψ has zero values for its x and z components, and non-zero y component ψ , as the SV wave lives in x – z plane. ϱ_+, ϱ_- and ϱ_{sh} are the ratios between the potential amplitudes of the fast P wave, the slow P wave and S wave in the fluid and solid part, respectively. Their derivations are given in Appendix B. As the poroelastic medium in Biot's theory is an effective medium, the solid and fluid are homogenized and are both present in the same space. This is the reason why an S wave potential appears in the fluid part (Wu *et al.* 1990). Assuming a flat horizontal interface, we chose a 2-D Cartesian coordinate system such that the x plane coincides with the interface separating the media, and we assume an incident plane fast P wave with a unit displacement amplitude and single angular frequency ω striking from the top half-space (see Fig. 1a).

In this case, the displacement potentials of the incident, reflected and transmitted waves are given by

$$\begin{cases} \phi_+^t = (e^{-i\gamma_+^t z} + B_+^t e^{i\gamma_+^t z}) e^{i(k_x x - \omega t)} \\ \phi_-^t = B_-^t e^{i\gamma_-^t z} e^{i(k_x x - \omega t)} \\ \psi^t = C^t e^{i\gamma_{sh}^t z} e^{i(k_x x - \omega t)} \\ \phi_+^b = B_+^b e^{-i\gamma_+^b z} e^{i(k_x x - \omega t)} \\ \phi_-^b = B_-^b e^{-i\gamma_-^b z} e^{i(k_x x - \omega t)} \\ \psi^b = C^b e^{-i\gamma_{sh}^b z} e^{i(k_x x - \omega t)}, \end{cases} \quad (10)$$

where $B_+^t, B_-^t, C^t, B_+^b, B_-^b, C^b$ are the R/T coefficients for the potential functions of the reflected fast P and slow P waves, the reflected S wave, the transmitted fast and slow P waves and the transmitted S wave, respectively. γ_+, γ_- and γ_{sh} are the z components of the corresponding wave vectors and the x component k_x is the same for different waves, according to Snell's law. They are given by

$$\begin{cases} k_x = \omega/V_+^t \sin\theta \\ k_x^2 + (\gamma_+^t)^2 = \omega^2/(V_+^t)^2 \\ k_x^2 + (\gamma_-^t)^2 = \omega^2/(V_-^t)^2 \\ k_x^2 + (\gamma_{sh}^t)^2 = \omega^2/(V_{sh}^t)^2 \\ k_x^2 + (\gamma_+^b)^2 = \omega^2/(V_+^b)^2 \\ k_x^2 + (\gamma_-^b)^2 = \omega^2/(V_-^b)^2 \\ k_x^2 + (\gamma_{sh}^b)^2 = \omega^2/(V_{sh}^b)^2, \end{cases} \quad (11)$$

where θ is the incidence angle (see Fig. 1) and V_+, V_-, V_{sh} are the velocities of the fast and the slow P waves and the S wave in the poroelastic medium, respectively. Combining eqs (10) and (11) with the equations of the interface conditions (6), and after simplification, we obtain the final linear system:

$$\mathbf{WX} = \mathbf{Z}, \quad (12)$$

where the 6-component vector $\mathbf{X} = [B_+^t \ B_-^t \ C^t \ B_+^b \ B_-^b \ C^b]^T$ contains the target R/T coefficients. Solving the linear system yields the R/T coefficients for the potential functions. To do this we use the built-in function *inv* in Matlab to invert the matrix \mathbf{W} . Detailed expressions and derivations of the matrix \mathbf{W} and the vector \mathbf{Z} , as well as the calculation of R/T coefficients for displacements instead of potentials are given in Appendix D. This system approach generalizes to any wave equation and choice of interface conditions, yielding a different system of equations for each case. When switching to the elastic/poroelastic interface, the pore-pressure continuity ($p^t = p^b$) condition does not apply and the number of equations and unknowns reduces to 5, as there are no slow P waves in the elastic half-space. For the acoustic/poroelastic interface, the number of equations and unknowns further reduces to 4, noting that then the conditions for continuity of normal and horizontal velocities in the solid part ($\dot{u}_z^t = \dot{u}_z^b$, $\dot{u}_x^t = \dot{u}_x^b$) do not apply, while the condition of continuity of normal relative velocity of the fluid to the frame ($\phi^t(\dot{U}_z^t - \dot{u}_z^t) = \phi^b(\dot{U}_z^b - \dot{u}_z^b)$) needs to be replaced by the conservation of the fluid volume ($\dot{U}_z^t = (1 - \phi^b)\dot{u}_z^b + \phi^b\dot{U}_z^b$).

2.5 Q compensation for waves propagating in the poroelastic medium

When dealing with an attenuating medium—due to either visco- or poroelasticity—it is important to note that the analytical R/T coefficients correspond to fields at the interface, while simulations resulting from a solver will often have source and receiver locations away from interfaces. In order to use R/T coefficients for benchmarking, one must take into account the attenuation effects due to propagation of the waves to and from the interface.

In our case, due to the viscosity of the fluid, waves propagating in the poroelastic medium are subject to attenuation, which can be characterized by the frequency-dependent quality factor $Q(\omega)$. For benchmarking purposes, we thus need to compensate for attenuation to obtain the displacements of the transmitted fast P wave and S wave right at the interface from the displacement records of receivers placed at a certain distance away from the interface. We denote the displacement in the frequency domain of a unit impulse traveling with the frequency-dependent velocity $V(\omega)$ at the position (x, z) as $\tilde{u}(x, z, \omega)$. Therefore, the displacement after propagation to $(x + x_0, z + z_0)$ for a distance L is given by

$$\tilde{u}(x + x_0, z + z_0, \omega) = \tilde{u}(x, z, \omega)e^{-\beta(\omega)L}e^{i\frac{\omega}{V(\omega)}L}, \quad (13)$$

where the frequency-dependent attenuation coefficient $\beta(\omega)$ is related to the quality factor $Q(\omega)$ by

$$\beta(\omega) = \frac{\omega}{2V(\omega)Q(\omega)}. \quad (14)$$

3 R/T -BASED BENCHMARKING

Using a 2-D geometry, we show that the interface conditions can indeed be used for numerical benchmarking, first, by comparing the R/T coefficients from plane-wave simulations against those calculated from plane-wave analysis, and secondly, by relying on point-source simulations only.

3.1 Plane-wave simulation

Plane-wave simulations do not involve geometrical spreading and therefore allow the straightforward calculation of R/T coefficients. The drawback is that they require multiple simulations, one for each desired angle of incidence, thus making this approach computationally expensive. This is especially true for larger angles, as a line source with a steep dipping angle is needed for each simulation, which in turn can often lead to large-aperture source arrays that require larger, laterally extended models. The line source and simulation time need to be long enough to separate the spherical waves originating from its two ends. Therefore in practice, the model size increases significantly with dipping angle. When the incidence angles are smaller than the critical angle, all the R/T coefficients are real-valued. At post-critical angles, the transmission coefficient of, for example the fast P wave becomes imaginary, therefore this wave becomes evanescent, propagating along the interface with its amplitude attenuating along the perpendicular direction in the lower half-space. We chose the elastic/poroelastic medium parameters resulting in a critical angle of 57.6° and show that the R/T coefficients match very well also for the post-critical angles of non-evanescent waves. Our study does not include evanescent wave behaviour, because of the difficulty in dealing with the superposition of the boundary reflection of the spherical direct wave after long simulation time. In principle, however, it is possible with our method to benchmark evanescent wave dynamics, if needed, by increasing computational resources.

3.1.1 Model setup

To illustrate our approach, we use a simple two-layer model comprising a top elastic medium and a bottom poroelastic medium (material parameters are listed in Table 2). The poroelastic parameters are taken from Morency & Tromp (2008). Fig. 3(a) shows the inverse quality factors for the fast P wave and S wave in the poroelastic medium and Figs 3(b) and (c) show the phase velocities of these two waves as a function of frequency, respectively. These quantities are required for the Q compensation (eq. 13). The slow P wave is not considered here due to its strong attenuation and very low transmission coefficient for the material parameters in Table 2.

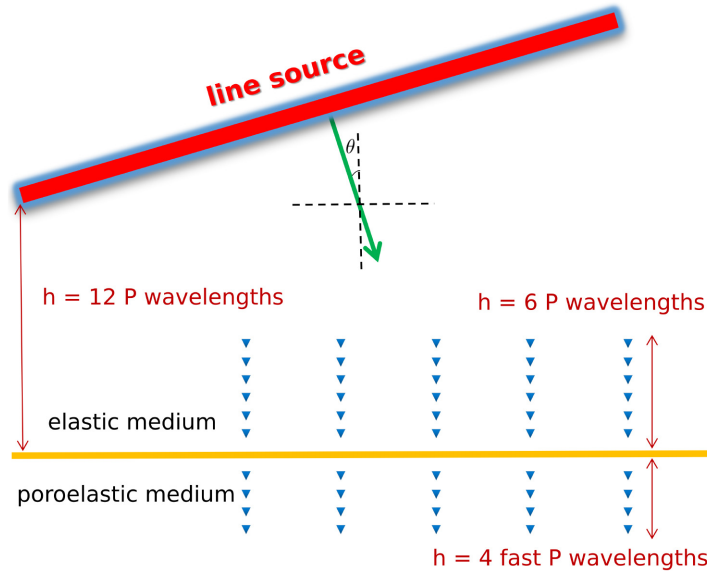


Figure 2. Illustration of the numerical setup for the plane-wave simulations. The thick red line represents the line source that generates the incident P wave with an incidence angle θ in the top half-space of the elastic medium. The blue triangles represent the array of receivers in both the top and bottom half-space to record the incident, reflected and transmitted waves.

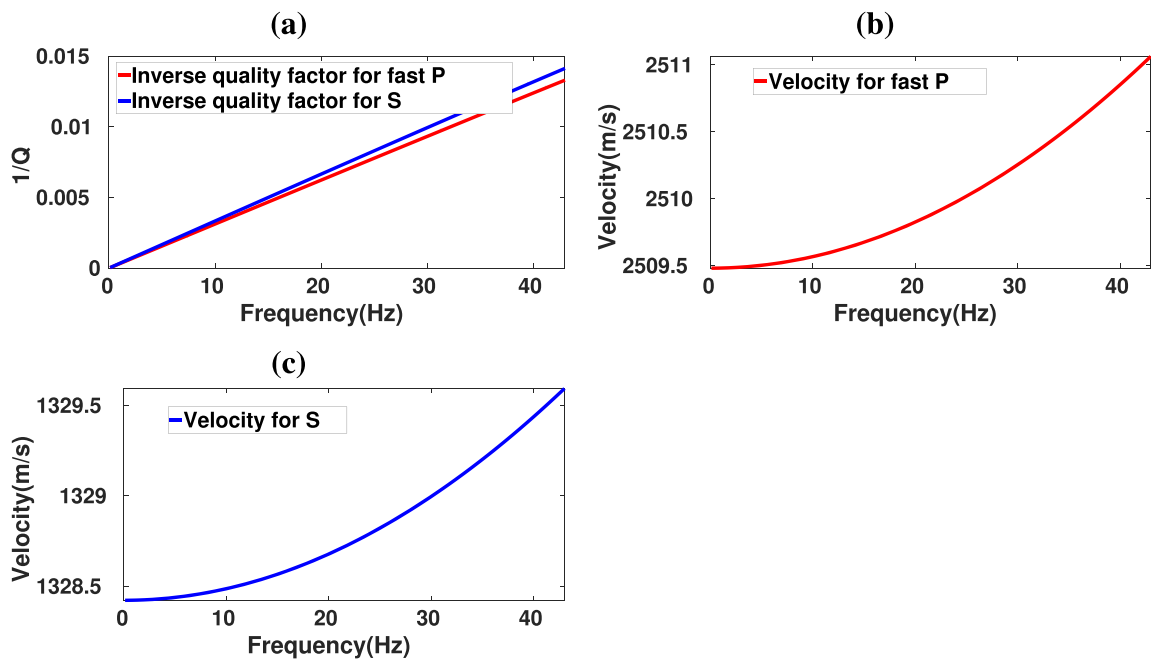


Figure 3. Dispersion properties in the poroelastic medium. (a) Frequency-dependent inverse quality factors of the fast P wave and S wave. (b and c) Corresponding frequency-dependent phase velocities. The red and blue solid lines represent the fast P wave and the S wave, respectively.

For the spectral element simulations, a line of explosive sources is placed in the elastic medium above the interface with a Ricker source of 15 Hz peak frequency, which generates an incident plane P wave that strikes the elastic/poroelastic interface. See Fig. 2 for more detailed illustration of the simulation setup. Five new waves result from the interaction of the incident P wave with the interface: the reflected P and S waves in the upper elastic medium, the transmitted fast and slow P waves as well as the transmitted S wave in the lower poroelastic medium, as shown in Fig. 1(b).

Arrays of receivers are placed on both sides of the interface and record the displacement components of each wave (see Fig. 2). To obtain R/T coefficients from these records, we select cases where the waves of interest are fully separable in space and time, from each other as well as from any residual artefacts that may be reflected from the artificial absorbing boundaries. For each identified wave, its corresponding displacement is a vector. We first apply the Q compensation in the frequency domain to the x and z components of the displacement vector. Then for each identified wave, we evaluate the total energy E of the wavelets to compute the absolute R/T coefficients of displacement (R_p ,

Table 2. Material parameters for plane-wave simulations.

Variable name	Symbol (Units)	Top layer (elastic)	Bottom layer (poroelastic)
<i>P</i> wave	V_p (m s ⁻¹)	2119	
<i>S</i> wave	V_s (m s ⁻¹)	1274	
Density	ρ (kg m ⁻³)	2650	
Fast <i>P</i> wave	V_+ (m s ⁻¹)		2509.7 ^a
Slow <i>P</i> wave	V_- (m s ⁻¹)		351.1 ^a
<i>S</i> wave	V_{sh} (m s ⁻¹)		1328.6 ^a
Solid density	ρ_s (kg m ⁻³)		2200
Fluid density	ρ_f (kg m ⁻³)		950
Tortuosity	c (–)		2
Porosity	ϕ (–)		0.4
Permeability	k (m ²)		1×10^{-10}
Solid bulk modulus	κ_s (GPa)		6.9
Fluid bulk modulus	κ_f (GPa)		2.0
Frame bulk modulus	κ_{fr} (GPa)		6.7
Fluid viscosity	η (Pa s)		0.001
Frame shear modulus	N (GPa)		3.0
Characteristic frequency	f_c (Hz)		335

Note: ^aPoroelastic wave speeds are frequency dependent and here they are calculated at 15 Hz.

R_s, T_{p1}, T_s) using

$$\left\{ \begin{array}{l} E = \sum_{i=t_e}^{i=t_b} u_x^2(i) + u_z^2(i) \\ R = \sqrt{\frac{E_{reflected}}{E_{incident}}} \\ T = \sqrt{\frac{E_{transmitted}}{E_{incident}}} \end{array} \right. \quad (15)$$

where t_b and t_e denote the begin and end time of the wavelets, respectively. As the transmitted slow *P* wave is diffusive together with a very low transmission coefficient, we are not considering it here. The R/T coefficients are calculated for multiple simulations for varying incidence angles ranging from 0° to 65° with a step of 5° with fixed space and time discretizations.

3.1.2 Elastic/poroelastic interface

To show angle-dependent effects of wave propagation, Figs 4(a)–(d) depict displacement wavefield snapshots for the incidence angles of 0°, 20°, 40° and 60°, respectively. For incidences smaller than the critical angle 57.6°, the reflected *P* and *S* waves and the transmitted fast *P* and *S* waves are present with amplitudes honouring the R/T coefficients shown in Fig. 5(a). The transmitted slow *P* wave is too weak to be identified, which is in line with the analytical prediction. At post-critical angles, the fast *P* wave transmission coefficients become complex, leading to an evanescent wave in the lower half-space, propagating horizontally along the interface with its amplitude decreasing exponentially in the perpendicular direction.

Figs 5(a)–(b) show the comparison between R/T coefficients from plan-wave analysis and the numerical simulations. The misfits for the two *S* waves in orange and blue at 0° are put to zero for visualization purpose as their corresponding theoretical R/T coefficients are zero and it is therefore meaningless to define a relative misfit. For most incidence angles, including the post-critical angles, the R/T coefficients match very well (relative misfits lower than 1.3 per cent) for R/T coefficients larger than 0.05. For very small R/T coefficients less than 0.004, the relative misfits increase, but that is foremost a numerical issue. For instance, the relative misfit of transmitted *S* wave coefficient (0.0038) at 5° is 3 per cent and the reflection coefficient (0.0026) for the *P* wave at 35° is 28 per cent. Amplitudes that are too small tend to cause large relative numerical errors.

Figs 6(a)–(b) as an example show different components of displacements used for calculating the reflection coefficients at 60°. Figs 7(a)–(b) show those used to calculate the transmission coefficients. Together we plot the *S* wave before and after Q compensation, also at 60°. To illustrate frequency dependent effects, Fig. 7(c) shows the amplitude spectrum of *x* component of the *S* waves before and after Q compensation, respectively. A phase shift occurs to the transmitted *S* wave, as can be seen by comparing the records in Figs 6 and 7.

3.2 Spherical-wave simulation

Plane-wave simulations are computationally demanding. It would be simpler, if we could instead use point source simulations. We therefore compare *P*-wave reflection coefficients for displacement obtained from explosive point source simulations against the reference coefficients

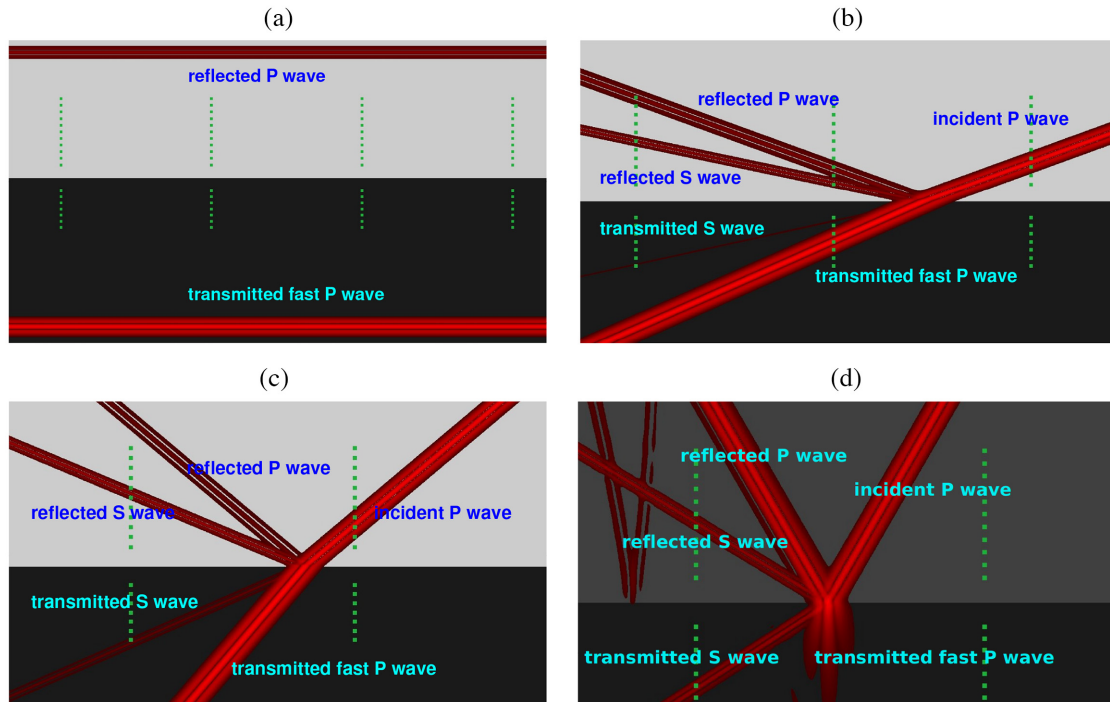


Figure 4. Plane-wave simulations for the elastic/poroelastic interface: (a)–(d) Cropped wavefield snapshots of the total displacement from the spectral element simulations with incidence angles of 0° , 20° , 40° and 60° , respectively. At the post-critical angle of 60° , the transmitted fast P wave becomes evanescent with a complex transmission coefficient. The green dots are the receivers.

obtained from plane-wave analysis for both, acoustic/poroelastic and elastic/poroelastic interfaces. We refrain from considering transmission coefficients, because of the complexity in correcting for geometrical spreading in poroelastic medium, mathematical expressions not available to us at the time of this work.

3.2.1 Model setup

The experiment setup for the point-source simulations is depicted in Fig. 8. An explosive source is placed horizontally in the middle of the two-layer model, $6P$ wavelengths above the interface in the acoustic or elastic medium. A line of receivers is placed at the same height as the source with each horizontal position defining a different incident angle, ranging from 0° to one degree below the critical angle. The source generates a P wave which strikes the interface and transmits a fast P wave, a slow P wave and S waves in the poroelastic medium and reflects P waves in the acoustic and P and S waves in the elastic medium. To retrieve the displacements at the interface from displacements recorded at a given receiver, thereby a specific incident angle, we need to undo geometrical spreading. We apply a factor \sqrt{d} for 2-D geometrical spreading to the direct wave as well as the reflected waves, where d is the distance along the path from the source (d for 3-D). The R/T coefficients are calculated in the same way as in eq. (15). The source time function we use for the simulations is a Ricker wavelet with 15 Hz peak frequency for the acoustic/poroelastic interface and different peak frequencies (5 Hz, 15 Hz, 40 Hz, 60 Hz and 80 Hz) for the elastic/poroelastic interface. We show in Table 3 the material parameters used for the simulations.

3.2.2 Acoustic/poroelastic interface

For the acoustic/poroelastic interface, we use the same material parameters as in Wu *et al.* (1990) with a critical angle of 35° . Fig. 9(a) shows the reference R/T coefficients for displacement obtained by plane-wave analysis and the P wave reflection coefficient from the spectral element simulation. The reflection coefficient is close to 0.4 below 20° and increases to 0.8 around the critical angle. The P wave reflection coefficients for the spectral element simulation agrees well that for incidence angles between 0° and 20° . The misfit, however, starts to increase drastically after 20° as the incidence angle approaches the critical angle. This discrepancy is due to finite-frequency interference of the strong head wave present in the modelled wavefield, which appears when the incidence wave strikes the interface at a vicinity of the critical angle. This head wave is of course not present in the plane-wave analysis and can't be undone from the simulations. In the following section, we show a case for the elastic/poroelastic interface without a strong headwave and the distortion near the critical angle is much less. The R/T coefficients assume a single-frequency plane-wave propagation at single reflection points, thus the finite-frequency time-domain nature of the simulation is responsible for the misfit. Because we rely on a finite-frequency Ricker wavelet, the reflection involves the complete corresponding Fresnel zone. For illustration, the wavefield snapshot of the vertical displacement component is shown in Fig. 9(b). The x and z components of records

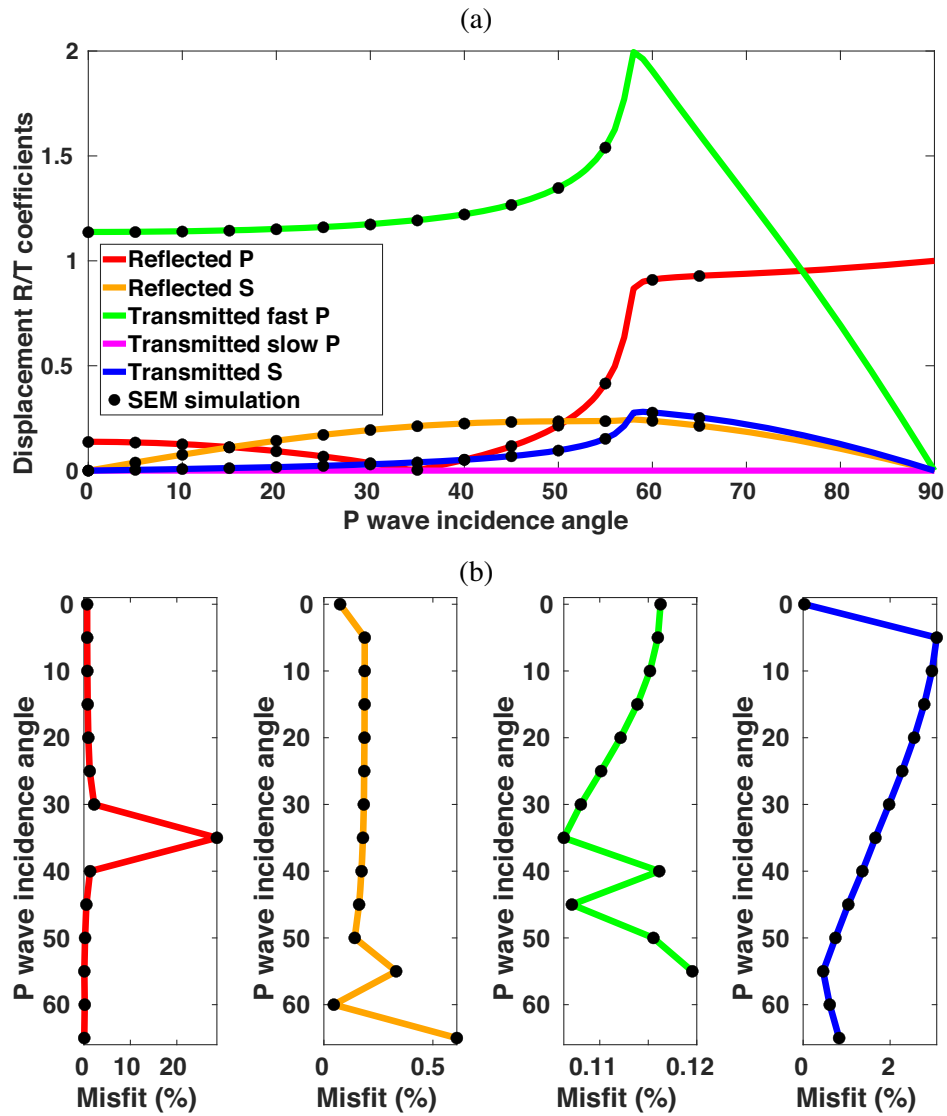


Figure 5. Plane-wave simulation for the elastic/poroelastic interface: (a) A comparison of the absolute reference reflection and transmission coefficients for displacement from plane-wave analysis (solid lines) and the spectral element simulations (dots) as a function of incidence angle. Red, orange, green and blue lines correspond to R_p , R_s , T_{p1} and T_s , respectively. The magenta line is the transmission coefficient of the transmitted slow P wave. After the critical angle of 57.6° , T_{p1} becomes complex and the transmitted fast P wave becomes evanescent. (b) The corresponding relative misfits in the same colour.

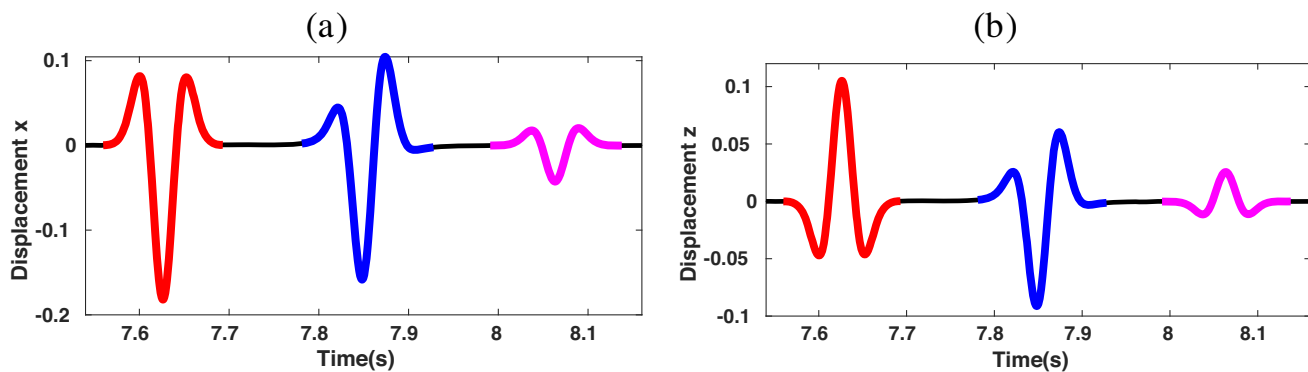


Figure 6. Plane-wave simulation for an incidence angle of 60° : (a)–(b) The x components, z components of displacements of the direct P wave (red), reflected P wave (blue) and reflected S wave (magenta), respectively.

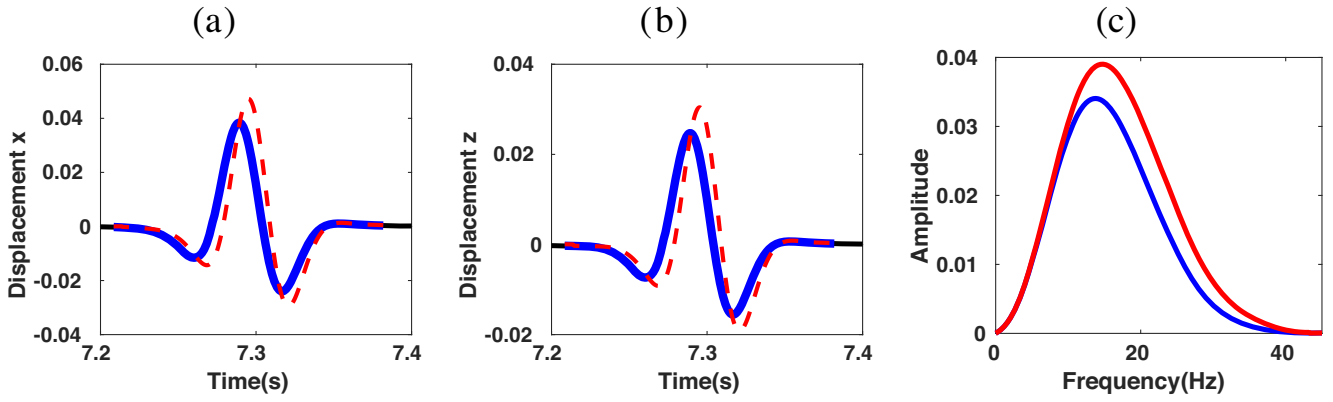


Figure 7. Plane-wave simulation for an incidence angle of 60° : (a)–(b) The x components and z components of the displacement vector of the transmitted S wave before (blue) and after (red) the Q compensation, respectively. (c) The frequency spectrum of the x component of transmitted S wave before (blue) and after (red) the Q compensation, respectively.

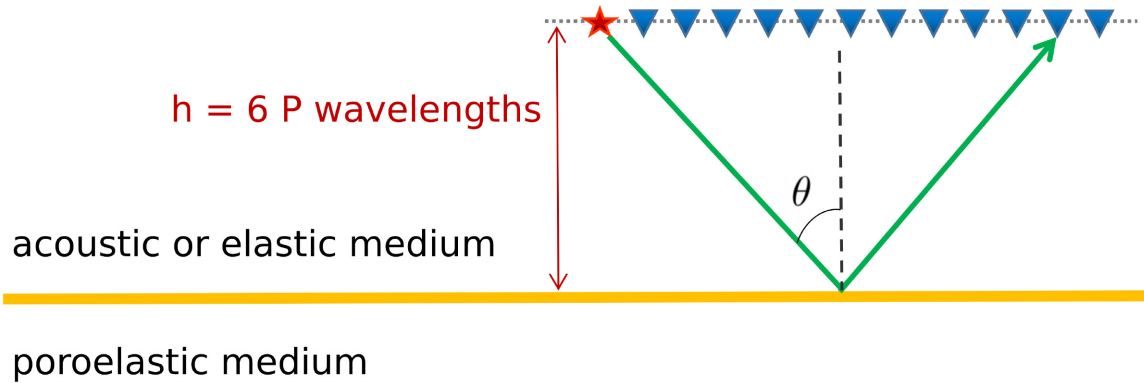


Figure 8. Illustration of the numerical experiment setup for the spherical-wave simulation. The red star and blue triangles in the top acoustic or elastic medium represent the source and receivers, located in a line which is $6P$ wavelengths from the interface. The horizontal coordinates of the receivers are decided by different incident P wave angles θ .

Table 3. Material parameters for spherical-wave simulations

Variable name	Symbol (Units)	Top layer (acoustic ^a)	Bottom layer (poroelastic ^a)	Top layer (elastic ^b)	Bottom layer (poroelastic ^b)
P wave	V_p (m s ⁻¹)	1500		2119	
S wave	V_s (m s ⁻¹)			1235	
Density	ρ (kg m ⁻³)	1000		2650	
Fast P wave	V_+ (m s ⁻¹)		2657		2693 ^c
Slow P wave	V_- (m s ⁻¹)		1280		1186 ^c
S wave	V_{sh} (m s ⁻¹)		1281		1410 ^c
Solid density	ρ_s (kg m ⁻³)		2480		2200
Fluid density	ρ_f (kg m ⁻³)		1000		950
Tortuosity	c (–)		1.79		2
Porosity	ϕ (–)		0.38		0.4
Permeability	k (m ²)		0		1×10^{-9}
Solid bulk modulus	κ_s (GPa)		49.9		6.9
Fluid bulk modulus	κ_f (GPa)		2.25		2.0
Frame bulk modulus	κ_{fr} (GPa)		5.17		6.7
Fluid viscosity	η (Pa s)		0		0.001
Frame bulk modulus	N (GPa)		2.80		3.0
Characteristic frequency	f_c (Hz)				335

Notes: ^aThe acoustic/poroelastic interface

^bThe elastic/poroelastic interface

^cPoroelastic wave speeds are frequency dependent and here they are calculated at 15 Hz.

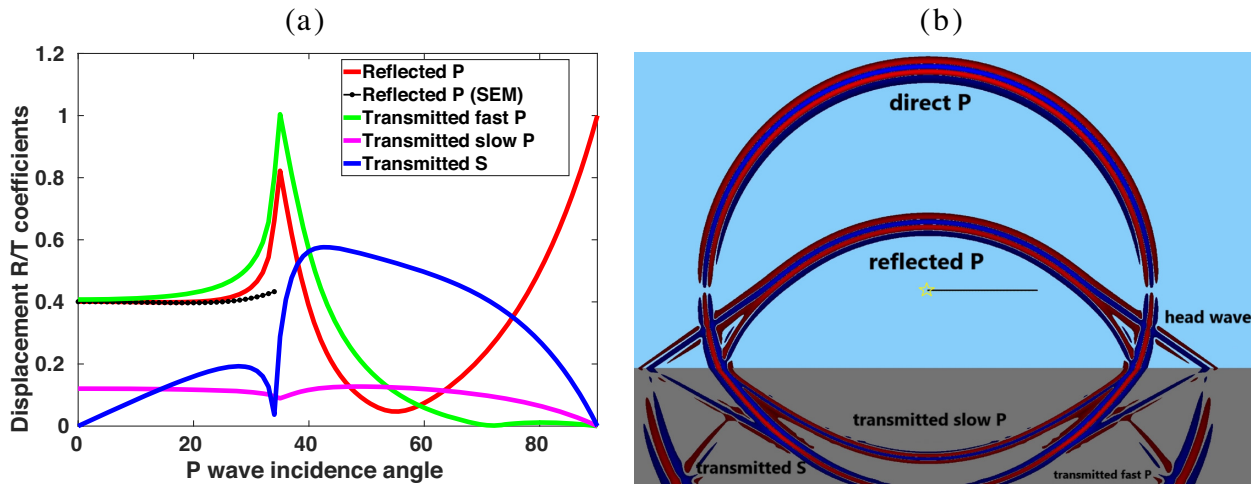


Figure 9. Spherical wave simulation for the acoustic/poroelastic interface: (a) A comparison of the absolute reference R/T coefficients of displacement from plane-wave analysis and P wave reflection coefficients from spectral element simulations (black dots) as a function of incidence angle. The red, green, magenta and blue solid lines denote the reference reflected P wave, the transmitted fast P , slow P and transmitted S waves, respectively. (b) Wavefield snapshot of the vertical displacement component from the spectral element modelling. The yellow star and black line represent the source and receivers, respectively.

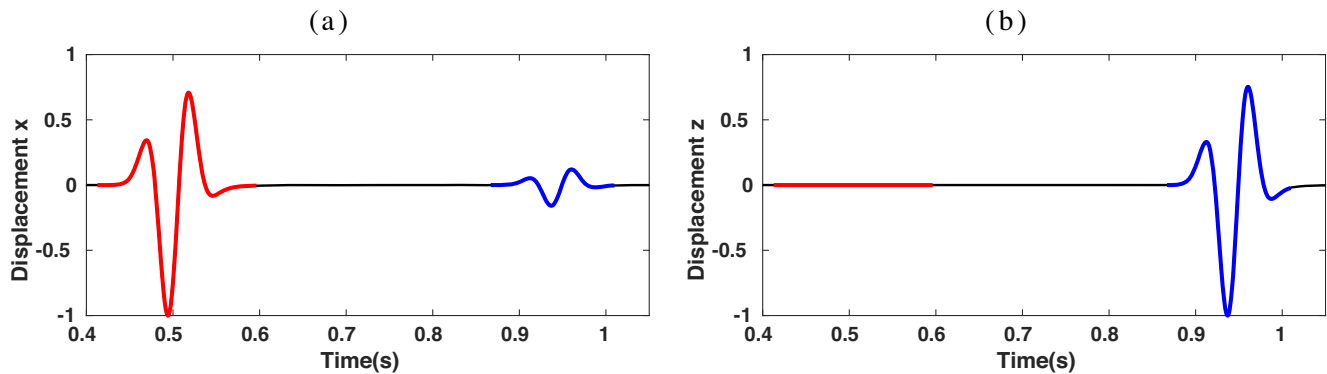


Figure 10. Spherical wave simulation of the acoustic/poroelastic interface: (a)–(b) The x components and z components of displacements of the direct P wave (red) and the reflected P wave (blue). The z component of the direct P wave is zero because it is propagating horizontally due to the locations of the receiver and source.

used to compute the P wave reflection coefficient are illustrated in Figs 10(a) and (b), for the incidence angle of 34° . The red and blue colours denote the direct and the reflected wave, respectively. The z component of the displacement of the direct P wave is zero because it is propagating horizontally due to the chosen source–receiver geometry.

3.2.3 Elastic/poroelastic interface

For the elastic/poroelastic interface, the material parameters are listed in Table 3 (Morency & Tromp 2008), yielding a critical angle of 55° . In this example, we run simulations for several peak Ricker frequencies (5 Hz, 15 Hz, 40 Hz, 60 Hz and 80 Hz) to study frequency-dependent effects.

Fig. 11(a) shows the absolute value of the reference R/T coefficients calculated from plane-wave analysis. The P wave reflection coefficient decreases from around 0.16 at zero incidence angle to almost zero at 38° and increases again to 0.22 around the critical angle. The wavefield snapshot of the total displacement is shown in Fig. 11(b). The reflected P and S waves in the elastic medium and the transmitted fast P wave, S wave in the poroelastic medium can be clearly identified. The transmitted slow P wave is too weak to be visible at this scale, which is expected given its relatively low transmission coefficient for the chosen medium parameters. It is worth noticing that in this case the head wave is also very weak compared to the previous case. Fig. 11(c) shows the comparison between P wave reflection coefficients for different angles obtained from spectral element simulations with different Ricker frequencies with those from plane-wave analysis. The corresponding relative misfits are shown separately in Fig. 11(d).

We observe that the numerical P -wave reflection coefficients for the elastic/poroelastic interface agree quite well with the interface-based predictions, except for incidence angles around 38° . This is because the reflection coefficient is relatively small (around 0.01) at this angle and here small absolute amplitude deviations can translate into relatively large percentage errors. When the incidence angle increases close to the critical angle at 55° , the relative misfit increases progressively to about 5 per cent, in contrast to the large misfit of more than 30 per cent

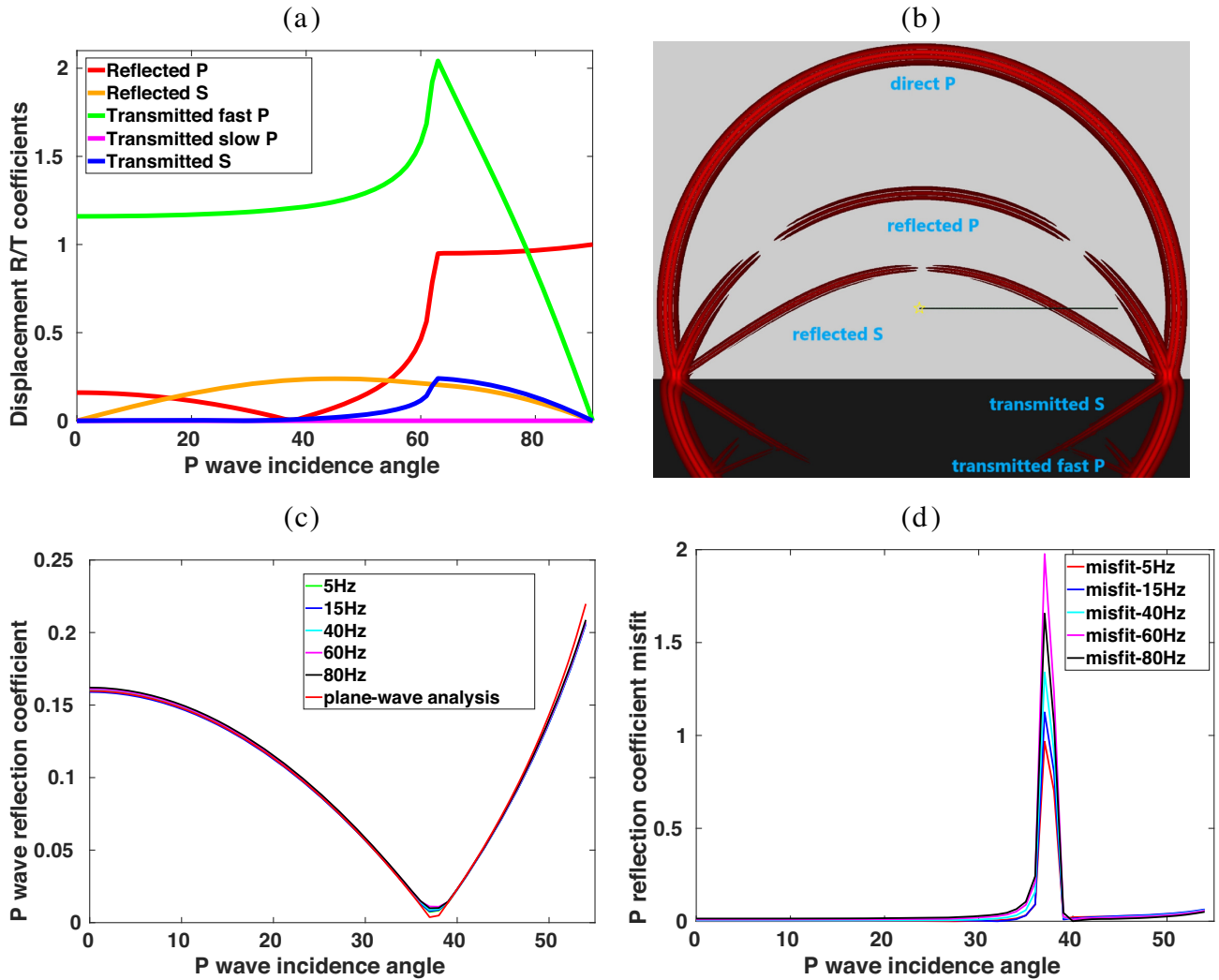


Figure 11. Spherical-wave simulation for the elastic/poroelastic interface: (a) The absolute reference R/T coefficients of displacement as a function of incidence angles. The red, orange, green, magenta and blue solid lines denote the reflected P and S waves, the transmitted fast P , slow P and transmitted S waves, respectively. (b) Wavefield snapshot of the total displacement component from spectral element modelling. The yellow star and black line represent the source and receivers, respectively. (c) Comparison of P -wave reflection coefficients for different frequencies of the source wavelet. (d) Relative misfits of P -wave reflection coefficients for different frequencies of the source wavelet.

in the acoustic/poroelastic case, where the energy of the head wave is considerably stronger compared to this example. For the frequency band from 5 to 80 Hz, generally used in exploration seismology, the relative misfits between the two methods remain relatively stable with the maximum lying within 1 per cent for small incidence angles below 30° . It is also possible to go beyond the critical angle here in this case given that the head wave energy is not very strong.

4 CONCLUSION

We show that a straightforward approach to benchmarking wavefield simulations in layered media is by comparing the R/T coefficients, either from the plane-wave analysis or point-source simulations. This is useful when no analytical Green's function is available, which is often the case for more complex media. To illustrate our approach, we provide numerical examples from SPEC-FEM2D in the case of coupled interfaces in porous media. We provide the necessary steps to compute reference reflection/transmission coefficients using plane-wave analysis, together with the processing steps for benchmarking numerical simulations. In principle, our method extends to 3-D and other complex wave systems incorporating, for example anisotropy, viscoelasticity, double porosities, partial saturation, two-phase fluids, the Biot/squirt flow, etc.

We show that the plane-wave analysis and the numerical simulations of plane-waves yield R/T coefficients for displacement with reasonably low relative misfits for angles well beyond the critical one and for all identifiable waves. The draw-back is that plane-wave simulations are computationally demanding.

Point source simulations are computationally easier, but need more involved processing to undo geometrical spreading before obtaining the R/T coefficients. They seem only useful for pre-critical angles as head-waves introduce finite frequency effects in the spherical wave reflection and transmission, which is difficult to correct.

Although we focus on poroelastic media, our benchmarking examples conclusively demonstrate that, for cases where the analytical Green's functions are not available, our general approach using R/T coefficients provides a flexible and reliable approach to benchmark any wave-equation solver.

ACKNOWLEDGEMENTS

This research is jointly supported by the China Scholarship Council (CSC) and the Utrecht Consortium for Subsurface Imaging (UCSI). We thank the Computational Infrastructure for Geodynamics (<http://geodynamics.org>) which is funded by the National Science Foundation under awards EAR-0949446 and EAR-1550901. We also thank Julien Diaz and Abdelaaziz Ezziani for releasing their code Gar6more2D online (<http://gar6more2d.gforge.inria.fr/>). In addition, we thank Alexey Stovas from the Norwegian University of Science and Technology for fruitful discussions. We thank Michael Afanasiev and Christina Morency for carefully reading and providing feedback on the manuscript. Data are available on request.

REFERENCES

- Albert, D.G., 1993. A comparison between wave propagation in water-saturated and air-saturated porous materials, *J. appl. Phys.*, **73**, 28.
- Biot, M.A., 1956. Theory of propagation of elastic waves in a fluid saturated porous solid. I. low frequency range, *J. acoust. Soc. Am.*, **28**, 168–191.
- Biot, M.A., 1962. Mechanics of deformation and acoustic propagation in porous media, *J. appl. Phys.*, **33**, 1482.
- Carcione, J.M., Morency, C. & Santos, J.E., 2010. Computational poroelasticity a review, *Geophysics*, **75**, 75A229–75A243.
- Corredor, R.M., Santos, J.E., Gauzellino, P.M. & Carcione, J.M., 2014. Reflection and transmission coefficients of a single layer in poroelastic media, *J. acoust. Soc. Am.*, **135**, 3151.
- Dai, N., Vafidis, A. & Kanasevich, E.R., 1995. Wave propagation in heterogeneous, porous media: a velocity-stress, finite-difference method, *Geophysics*, **60**, 327–340.
- de la Puente, J., Dumbser, M., Käser, M. & Igel, H., 2008. Discontinuous galerkin methods for wave propagation in poroelastic media, *Geophysics*, **73**, T77–T97.
- Denneeman, A.I.M., Drijkoningen, G.G., Smeulders, D.M.J. & Wapenaar, K., 2002. Reflection and transmission of waves at a fluid/porous-medium interface, *Geophysics*, **67**, 282–291.
- Deresiewicz, H. & Skalak, R., 1963. On uniqueness in dynamic poroelasticity, *Bull. seism. Soc. Am.*, **53**, 783–788.
- Diaz, J. & Ezziani, A., 2008a. Analytical solution for waves propagation in heterogeneous acoustic/porous media. part I: the 2D case, *Commun. Computat. Phys.*, **7**(1), 171–194.
- Diaz, J. & Ezziani, A., 2008b. Analytical solution for wave propagation in stratified poroelastic medium. part I: the 2D case, Research Report, RR-6591, INRIA., p. 27.
- Diaz, J. & Ezziani, A., 2008c. Analytical solution for wave propagation in stratified poroelastic medium. part II: the 3-D case, Research Report, RR-6595, INRIA., p. 40.
- Diaz, J. & Ezziani, A., 2009. Analytical solution for wave propagation in stratified acoustic/porous media. part II: the 3D case, *Commun. Computat. Phys.*, **7**(3), 445–472.
- Diaz, J. & Ezziani, A., 2013. Gar6more2D [software].
- Dupuy, B., Barros, L.D., Garambois, S. & Virieux, J., 2011. Wave propagation in heterogeneous porous media formulated in the frequency-space domain using a discontinuous Galerkin method, *Geophysics*, **76**, N13–N28.
- Dutta, N.C. & Odé, H., 1983. Seismic reflections from a gas-water contact, *Geophysics*, **48**, 148–162.
- Feng, S. & Johnson, D.L., 1983. High-frequency acoustic properties of a fluid/porous solid interface. I. New surface mode, *J. acoust. Soc. Am.*, **74**, 906.
- Gurevich, B., 1996. Numerical simulation of ultrasonic experiments on poroelastic samples, in *Proceedings of the 58th EAGE Conference and Exhibition, Extended Abstracts*, EAGE.
- Gurevich, B. & Schoenberg, M., 1999. Interface conditions for Biot's equations of poroelasticity, *J. acoust. Soc. Am.*, **105**, 2585.
- Haffinger, P., Eyvazi, F.J., Steeghs, P., Doulgeris, P., Gisolf, D. & Verschuur, E., 2018. Quantitative prediction of injected CO₂ at Sleipner using wave-equation based AVO, in *Proceedings of the Fifth CO₂ Geological Storage Workshop*, November 2018, Vol. 2018, pp. 1–5, doi:10.3997/2214-4609.201802997, European Association of Geoscientists & Engineers.
- Komatitsch, D., et al., 2012. SPECSEM2D v7.0.0 [software].
- Kumari, M., Barak, M. & Kumar, M., 2017. Seismic reflection and transmission coefficients of a single layer sandwiched between two dissimilar poroelastic solids, *Petrol. Sci.*, **14**, 676–693.
- Lumley, D., 2010. 4D seismic monitoring of CO₂ sequestration, *Leading Edge*, **29**, 113–240.
- Masson, Y.J. & Pride, S.R., 2007. Poroelastic finite difference modeling of seismic attenuation and dispersion due to mesoscopic-scale heterogeneity, *J. geophys. Res.*, **112**, B03204.
- Masson, Y.J. & Pride, S.R., 2010. Finite-difference modeling of Biot's poroelastic equations across all frequencies, *Geophysics*, **75**, N33–N41.
- Masson, Y.J., Pride, S.R. & Nihei, K.T., 2006. Finite difference modeling of Biot's poroelastic equations at seismic frequencies, *J. geophys. Res.*, **111**, B10305.
- Molotkov, L.A., 2002. On the coefficients of pore tortuosity in the effective Biot model, *J. Math. Sci.*, **108**, 752–757.
- Morency, C., Luo, Y. & Tromp, J., 2011. Acoustic, elastic and poroelastic simulations of CO₂ sequestration crosswell monitoring based on spectral-element and adjoint methods, *Geophys. J. Int.*, **185**, 955–966.
- Morency, C. & Tromp, J., 2008. Spectral-element simulations of wave propagation in porous media, *Geophys. J. Int.*, **175**, 301–345.
- Peng, H., Sripanich, Y., Vasconcelos, I. & Trampert, J., 2018. A comparison of reflection coefficients in porous media from 2D plane-wave analysis and spectral-element forward modeling, *SEG Technical Program Expanded Abstracts*, 3974–3978.
- Quiroga-Goode, G., 2005. Coupling biot wave equation with de la Cruz and Spanos boundary conditions for multi-layered porous systems, *Bull. Geofis. Teor. Appl.*, **46**, 287–302.
- Rasolofosaon, P.N.J., 1988. Importance of interface hydraulic condition on the generation of second bulk compressional wave in porous media, *Wave Motion*, **52**, 780.
- Santos, J.E., Corbero, J.M., Ravazzoli, C.L. & Hensley, J.L., 1992. Reflection and transmission coefficients in fluid-saturated porous media, *J. acoust. Soc. Am.*, **91**, 1911.
- Sharma, M.D. & Gogna, M.L., 1992. Reflection and refraction of plane harmonic waves at an interface between elastic solid and porous solid saturated by viscous liquid, *Pure appl. Geophys.*, **138**, 0033–4553.

- Stein, S. & Wysession, M., 2003. *An Introduction to Seismology, Earthquakes, and Earth Structure*, Blackwell Publishing.
- Stoll, R.D. & Kan, T.K., 1981. Reflection of acoustic waves at a water-sediment interface, *J. acoust. Soc. Am.*, **70**, 149.
- Tromp, J., Komatitsch, D. & Liu, Q., 2008. Spectral-element and adjoint methods in seismology, *Commun. Comput. Phys.*, **3**(1), 1–32.
- Ursenbach, C.P., Haase, A.B. & Downton, J.E., 2007. Efficient spherical-wave AVO modeling, *Leading Edge*, **26**, 1584–1589.
- Vashishth, A.K. & Sharma, M.D., 2009. Reflection and refraction of acoustic waves at poroelastic ocean bed, *Earth. Planets. Space.*, **61**, 675–687.
- Vashishth, A.K., Sharma, M.D. & Gogna, M.L., 1991. Reflection and transmission of elastic waves at a loosely bonded interface between an elastic solid and liquid-saturated porous solid, *Geophys. J. Int.*, **105**, 601–617.
- Virieux, J. & Operto, S., 2009. An overview of full-waveform inversion in exploration geophysics, *Geophysics*, **74**, WCC127–WCC152.
- Wenzlau, F. & Müller, T.M., 2009. Finite-difference modeling of wave propagation and diffusion in poroelastic media, *Geophysics*, **74**, T55–T66.
- Wu, K., Xue, Q. & Adler, L., 1990. Reflection and transmission of elastic waves from a fluid-saturated porous solid boundary, *J. acoust. Soc. Am.*, **87**, 2349.
- Yang, J., 1999. Importance of flow condition on seismic waves at a saturated porous solid boundary, *J. Sound. Vib.*, **221**, 391–413.
- Yeh, C.-L., Lo, W.-C., Jan, C.-D. & Yang, C.-C., 2010. Reflection and refraction of obliquely incident elastic waves upon the interface between two porous elastic half-spaces saturated by different fluid mixtures, *J. Hydrol.*, **395**, 91–102.
- Zhang, Y. & Gao, J., 2014. A 3D staggered-grid finite difference scheme for poroelastic wave equation, *J. appl. Geophys.*, **109**, 281–291.

APPENDIX A: GREEN’S-FUNCTION-BASED BENCHMARKING

Perhaps the most straightforward way to benchmark a wave-equation solver is to compare its numerical point-source solution to an analytical Green’s function convolved with the band-limited source wavelet used in the simulation. However, this is only possible for very limited cases because deriving analytical Green’s functions for complex media is challenging, and they are only available in the literature for certain wave operators and media. In most cases they are limited to homogeneous media, or occasionally to two-layer homogeneous models. Below, we focus on the special case of analytical Green’s function for the 2-D open-pore elastic/poroelastic interface with zero viscosity. An analytical Green’s function has not been derived yet for this case to our knowledge.

To this end, we point out that the theory of poroelasticity naturally reduces to elasticity when (i) the porosity parameter ϕ decreases to zero and when (ii) the frame bulk modulus equals that of the solid, because of the consistency. Therefore, the elastic/poroelastic interface can be approximated by a poroelastic/poroelastic interface using these specific parameter settings. We use the open-source code Gar6more2D (Diaz & Ezziani 2013) to generate the analytical Green’s function, although the porosity parameter is only allowed to have non-zero values. We show that the elastic/poroelastic interface can effectively be obtained by utilizing the analytical Green’s function for the poroelastic/poroelastic interface, where the elastic medium is approximated by setting the porosity to a very small value (0.0000001) with material parameters listed in Table A1. A justification of this approximation based on the R/T coefficients is given in Fig. A1 with the same material parameters. As can be seen, these two plane-wave analyses yield comparable results, a consequence of consistency between elasticity and the limiting case of poroelasticity. We acknowledge that in theory our Green’s function example is based on a false assumption of extremely small porosity to mimic the elastic solution. But owing to the consistency between poroelasticity and elasticity, the misfit is small enough to be negligible.

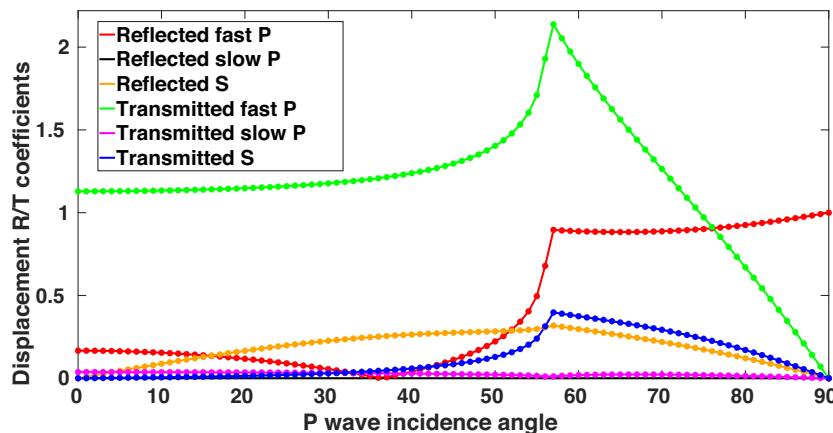


Figure A1. A comparison of the absolute displacement R/T coefficients obtained from plane-wave analyses for the elastic/poroelastic interface and the poroelastic/poroelastic interface with material parameters listed in Table A1. In both cases the lower poroelastic layer is set to be the same. Note that the upper elastic layer is in one case approximated by a poroelastic layer by setting the porosity to be 0.0000001 and the frame modulus equal to the bulk modulus. For the poroelastic/poroelastic interface, the solid red, black, yellow, blue, magenta, and cyan lines denote the R/T coefficients of the reflected fast P , slow P , S , transmitted fast P , slow P and S waves, respectively. For the proper elastic/poroelastic interface, the dots in the same colour denote the corresponding R/T coefficients of the reflected P , S , transmitted fast P , slow P and S waves.

For the spectral element simulation, we choose the same model setup used in fig. 13 of Morency & Tromp (2008) with a top elastic layer and a bottom poroelastic layer. The dimensions of the model is $4800 \text{ m} \times 4800 \text{ m}$ with an explosive source placed in the top layer at $x_s = (1600, 2900)$. The source–time function is Ricker wavelet with a dominant frequency of 15 Hz. Two receivers are placed separately in the two different layers at $x_{r1} = (2000, 3200)$ and $x_{r2} = (2000, 1867)$ to record the reflected and transmitted waves, respectively. Fig. A2(a)

Table A1. Material Parameters

Variable name	Symbol (Units)	Top layer (elastic ^a)	Top layer (poroelastic ^b)	Bottom layer (poroelastic)
<i>P</i> wave	V_p (m s ⁻¹)	2240		
<i>S</i> wave	V_s (m s ⁻¹)	1337		
Density	ρ (kg m ⁻³)	2600		
Fast <i>P</i> wave	V_+ (m s ⁻¹)		2240	2693
Slow <i>P</i> wave	V_- (m s ⁻¹)		1219	1186
<i>S</i> wave	V_{sh} (m s ⁻¹)		1337	1410
Solid density	ρ_s (kg m ⁻³)		2600	2200
Fluid density	ρ_f (kg m ⁻³)		950	950
Tortuosity	c (-)		2	2
Porosity	ϕ (-)		0.0000001	0.4
Permeability	k (m ²)		1×10^{-10}	1×10^{-10}
Solid bulk modulus	κ_s (GPa)		6.845	6.9
Fluid bulk modulus	κ_f (GPa)		2.0	2.0
Frame bulk modulus	κ_{fr} (GPa)		6.845	6.7
Fluid viscosity	η (Pa s)		0	0
Frame shear modulus	N (GPa)		4.652	3.0

Notes: The poroelastic medium^b is approximately equal to the elastic medium^a by setting the porosity to 0.0000001

and the frame modulus equal to the bulk modulus. It is used for generating the analytical Green's function in Fig. A2 and the plane-wave analysis of the poroelastic/poroelastic interface in Fig. A1.

shows the wavefield snapshot of the vertical-component displacement at $t = 0.8$ s, where different reflected and transmitted waves can be observed. Figs A2(b) and (c) show the comparison of the vertical particle velocity for the two receivers for the spectral element simulation and the analytical solution. The misfit shows that they are indeed very close. We admit that the misfit around 0.55 s in Fig. A2(b) could be the direct slow *P* wave, but with negligible amplitude.

APPENDIX B: DERIVATION OF q_+ , q_- , q_{sh}

The derivations of parameters q_+ , q_- , q_{sh} in eq. (9) are given below based on Yang (1999), where a different, but equivalent set of Biot's wave equations in the form of displacement \mathbf{u} in the solid and the relative displacement of the fluid to the solid \mathbf{w} is used (Biot 1962):

$$\begin{cases} (\lambda + \mu + \alpha^2 M) \nabla(\nabla \cdot \mathbf{u}) + \mu \nabla^2 \mathbf{u} + \alpha M \nabla(\nabla \cdot \mathbf{w}) = \rho \frac{\partial^2 \mathbf{u}}{\partial t^2} + \rho_f \frac{\partial^2 \mathbf{w}}{\partial t^2} \\ \alpha M \nabla(\nabla \cdot \mathbf{u}) + M \nabla(\nabla \cdot \mathbf{w}) = \rho_f \frac{\partial^2 \mathbf{u}}{\partial t^2} + m \frac{\partial^2 \mathbf{w}}{\partial t^2} + b \frac{\partial \mathbf{w}}{\partial t} \end{cases} \quad (\text{B1})$$

with \mathbf{w} defined as

$$\mathbf{w} = \phi(\mathbf{U} - \mathbf{u}) \quad (\text{B2})$$

λ and μ are the Lamé constants of the solid skeleton. The other parameters are given by

$$\begin{cases} \rho = (1 - \phi)\rho_s + \phi\rho_f \\ \alpha = 1 - \frac{\kappa_{fr}}{\kappa_s} \\ M = 1 - \frac{\kappa_s^2}{\kappa_d - \kappa_{fr}} \\ \kappa_d = \kappa_s \left[1 + \phi \left(\frac{\kappa_s}{\kappa_f} - 1 \right) \right] \\ m = c\rho_f/\phi \\ b = \eta/k. \end{cases} \quad (\text{B3})$$

A Helmholtz solution of the two displacement vectors is used in the plane-wave analysis:

$$\begin{cases} \mathbf{u} = \nabla\phi_s + \nabla \times \Psi_s \\ \mathbf{w} = \nabla\phi_f + \nabla \times \Psi_f. \end{cases} \quad (\text{B4})$$

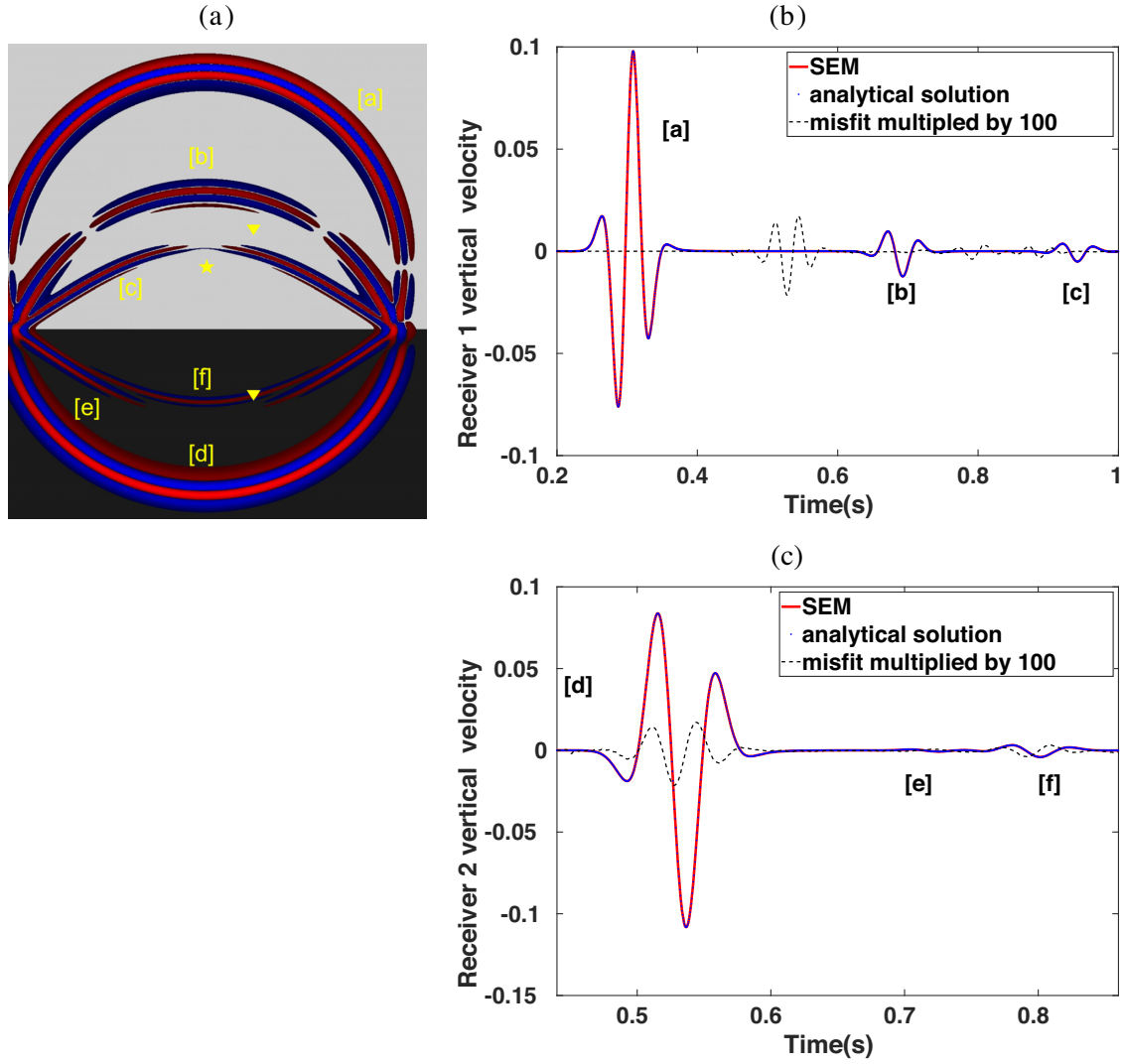


Figure A2. Simulation of wave propagation in a model consisting of a homogeneous poroelastic layer beneath a homogeneous elastic layer, as tabulated in Table A1. The model dimensions are $4800 \text{ m} \times 4800 \text{ m}$, the source (yellow star) is located at $\mathbf{x}_s = (1600, 2900)$ and the receivers (yellow triangles) at $\mathbf{x}_{r1} = (2000, 3200)$ and $\mathbf{x}_{r2} = (2000, 1867)$. The explosive source has a Ricker wavelet source–time function with a dominant frequency of 15 Hz. (a) Snapshot of the vertical-component velocity at $t = 0.8 \text{ s}$, where the direct fast P ([a]), the reflected P ([b]), the reflected S ([c]), the transmitted fast P ([d]), the transmitted slow P ([e]) and the transmitted S ([f]) can be clearly observed. (b) and (c) records of vertical-component velocity of receivers 1 and 2 in the upper elastic layer and the lower poroelastic layer, respectively. The solid red and blue dotted lines show the results from SEM and analytical solution, respectively. The black dots show the misfit between them multiplied by 100.

Similar to Ψ in eq. (9), we have $\Psi_s = [0, \psi_s, 0]$ and $\Psi_f = [0, \psi_f, 0]$. The potential functions are given by

$$\begin{cases} \phi_s = A_{s1}e^{i(\omega t - l_{1x}x - l_{1z}z)} + A_{s2}e^{i(\omega t - l_{2x}x - l_{2z}z)} \\ \phi_f = A_{f1}e^{i(\omega t - l_{1x}x - l_{1z}z)} + A_{f2}e^{i(\omega t - l_{2x}x - l_{2z}z)} \\ \psi_s = B_s e^{i(\omega t - l_{sx}x - l_{sz}z)} \\ \psi_f = B_f e^{i(\omega t - l_{fx}x - l_{fz}z)}, \end{cases} \quad (\text{B5})$$

where the indices 1, 2, s denote fast P wave, slow P wave and S wave, respectively. Solving the following characteristic equations yields the wave vectors of fast P wave, slow P wave and S wave l_1, l_2 (together denoted by l_p) and l_s .

$$\begin{vmatrix} \rho\omega^2 - (\lambda + 2\mu + \alpha^2 M)l_p^2 & \rho_f\omega^2 - \alpha^2 M l_p^2 \\ \rho_f\omega^2 - \alpha^2 M l_p^2 & m\omega^2 - \alpha^2 M l_p^2 - i b\omega \end{vmatrix} = 0 \quad (\text{B6})$$

$$\begin{vmatrix} \rho\omega^2 - \mu l_s^2 & \rho_f\omega^2 \\ \rho_f\omega^2 & m\omega^2 - i b\omega \end{vmatrix} = 0. \quad (\text{B7})$$

The ratio between the amplitudes of the potential functions for the fast P wave, the slow P wave and the S wave are given by the following equations, respectively:

$$\begin{cases} \delta_1 = \frac{A_{f1}}{A_{s1}} = \frac{(\lambda_c + 2\mu)l_1^2 - \rho\omega^2}{\rho_f\omega^2 - \alpha^2 M l_1^2} \\ \delta_2 = \frac{A_{f2}}{A_{s2}} = \frac{(\lambda_c + 2\mu)l_2^2 - \rho\omega^2}{\rho_f\omega^2 - \alpha^2 M l_2^2} \\ \delta_s = \frac{B_f}{B_s} = \frac{\mu l_s^2 - \rho\omega^2}{\rho_f\omega^2}, \end{cases} \quad (\text{B8})$$

where $\lambda_c = \lambda + \alpha^2 M$. Below we show that the coefficients ϱ_+ , ϱ_- , ϱ_{sh} in eq. (9) can be calculated directly from δ_1 , δ_2 and δ_s , respectively, by using the relation between \mathbf{w} , \mathbf{u} and \mathbf{U} . We have

$$\mathbf{w} = \nabla\phi_f + \nabla \times \Psi_f = \phi(\mathbf{U} - \mathbf{u}) = \phi(\mathbf{U} - \nabla\phi_s - \nabla \times \Psi_s). \quad (\text{B9})$$

While keeping Ψ_f and Ψ_s in the vector form explicit for simpleness, \mathbf{U} is expressed as

$$\begin{aligned} \mathbf{U} &= \frac{1}{\phi} \nabla\phi_f + \nabla\phi_s + \frac{1}{\phi} \nabla \times \Psi_f + \nabla \times \Psi_s \\ &= \frac{1}{\phi} \nabla\phi_f + \nabla\phi_s + \frac{1}{\phi} \nabla \times [0, \psi_f, 0] + \nabla \times [0, \psi_s, 0] \\ &= \frac{1}{\phi} \nabla [A_{f1} e^{i(\omega t - l_{1x}x - l_{1z}z)} + A_{f2} e^{i(\omega t - l_{2x}x - l_{2z}z)}] + \nabla [A_{s1} e^{i(\omega t - l_{1x}x - l_{1z}z)} + \\ &\quad A_{s2} e^{i(\omega t - l_{2x}x - l_{2z}z)}] + \frac{1}{\phi} \nabla \times [0, B_f e^{i(\omega t - l_{sx}x - l_{sz}z)}, 0] + \nabla \times [0, B_s e^{i(\omega t - l_{sx}x - l_{sz}z)}, 0]. \end{aligned} \quad (\text{B10})$$

Reorganizing all the terms, we have

$$\begin{aligned} \mathbf{U} &= \left[\frac{1}{\phi} \nabla A_{f1} e^{i(\omega t - l_{1x}x - l_{1z}z)} + \nabla A_{s1} e^{i(\omega t - l_{1x}x - l_{1z}z)} \right] + \left[\frac{1}{\phi} \nabla A_{f2} e^{i(\omega t - l_{2x}x - l_{2z}z)} + \right. \\ &\quad \left. \nabla A_{s2} e^{i(\omega t - l_{2x}x - l_{2z}z)} \right] + \frac{1}{\phi} \nabla \times [0, B_f e^{i(\omega t - l_{sx}x - l_{sz}z)}, 0] + \nabla \times [0, B_s e^{i(\omega t - l_{sx}x - l_{sz}z)}, 0]. \end{aligned} \quad (\text{B11})$$

Note we have $A_{f1} = \delta_1 A_{s1}$, $A_{f2} = \delta_2 A_{s2}$ and $B_f = \delta_s B_s$. So

$$\begin{aligned} \mathbf{U} &= \left[\frac{1}{\phi} \nabla \delta_1 A_{s1} e^{i(\omega t - l_{1x}x - l_{1z}z)} + \nabla A_{s1} e^{i(\omega t - l_{1x}x - l_{1z}z)} \right] + \left[\frac{1}{\phi} \nabla \delta_2 A_{s2} e^{i(\omega t - l_{2x}x - l_{2z}z)} + \right. \\ &\quad \left. \nabla A_{s2} e^{i(\omega t - l_{2x}x - l_{2z}z)} \right] + \frac{1}{\phi} \nabla \times [0, \delta_s B_s e^{i(\omega t - l_{sx}x - l_{sz}z)}, 0] + \nabla \times [0, B_s e^{i(\omega t - l_{sx}x - l_{sz}z)}, 0] \\ &= \left(\frac{\delta_1}{\phi} + 1 \right) \nabla A_{s1} e^{i(\omega t - l_{1x}x - l_{1z}z)} + \left(\frac{\delta_2}{\phi} + 1 \right) \nabla A_{s2} e^{i(\omega t - l_{2x}x - l_{2z}z)} + \\ &\quad \left(\frac{\delta_s}{\phi} + 1 \right) \nabla \times [0, B_s e^{i(\omega t - l_{sx}x - l_{sz}z)}, 0]. \end{aligned} \quad (\text{B12})$$

Note there are corresponding relations between ϕ_+ , ϕ_s and ϕ_f , between ϕ_- , ϕ_s and ϕ_f , between ψ , ψ_s and ψ_f

$$\begin{cases} \phi_+ = A_{s1} e^{i(\omega t - l_{1x}x - l_{1z}z)} \\ \phi_- = A_{s2} e^{i(\omega t - l_{2x}x - l_{2z}z)} \\ \psi = B_s e^{i(\omega t - l_{sx}x - l_{sz}z)}. \end{cases} \quad (\text{B13})$$

Using the above relations, \mathbf{U} can be further expressed in terms of ϕ_+ , ϕ_- and Ψ as

$$\mathbf{U} = \left(\frac{\delta_1}{\phi} + 1 \right) \nabla\phi_+ + \left(\frac{\delta_2}{\phi} + 1 \right) \nabla\phi_- + \left(\frac{\delta_s}{\phi} + 1 \right) \nabla \times \Psi. \quad (\text{B14})$$

Comparing with eqs (9), we therefore have

$$\begin{cases} \varrho_+ = - \left(\frac{\delta_1}{\phi} + 1 \right) \\ \varrho_- = - \left(\frac{\delta_2}{\phi} + 1 \right) \\ \varrho_{sh} = \left(\frac{\delta_s}{\phi} + 1 \right). \end{cases} \quad (\text{B15})$$

APPENDIX C: INTERFACE CONDITIONS IN POROUS MEDIA

The equations corresponding to the elastic/poroelastic and acoustic/poroelastic interface conditions in Table 1 are as follows:

C1 Elastic/poroelastic interface

In the elastic medium, σ_{zz} , σ_{xz} , \dot{u}_z and \dot{u}_x stand for stress and velocity, respectively.

$$\begin{cases} \sigma_{zz}^t = \sigma_{zz}^b - \phi^b p^b \\ \sigma_{xz}^t = \sigma_{xz}^b \\ \dot{u}_z^t = \dot{u}_z^b \\ \dot{u}_x^t = \dot{u}_x^b \\ \dot{U}_z^b = \dot{u}_z^b. \end{cases} \quad (C1)$$

The equations with the corresponding constitutive relations are

$$\begin{cases} \lambda^t \frac{\partial u_x^t}{\partial x} + (\lambda^t + 2\mu^t) \frac{\partial u_z^t}{\partial z} = (P^b - 2N^b + Q^b) \frac{\partial u_x^b}{\partial x} + (P^b + Q^b) \frac{\partial u_z^b}{\partial z} \\ \quad + (Q^b + R^b)(\nabla \cdot U^b) \\ \mu^t \left(\frac{\partial u_z^t}{\partial x} + \frac{\partial u_x^t}{\partial z} \right) = N^b \left(\frac{\partial u_z^b}{\partial x} + \frac{\partial u_x^b}{\partial z} \right) \\ \dot{u}_z^t = \dot{u}_z^b \\ \dot{u}_x^t = \dot{u}_x^b \\ \dot{U}_z^b = \dot{u}_z^b. \end{cases} \quad (C2)$$

C2 Acoustic/poroelastic interface

In the acoustic medium, p , \dot{U}_z , κ_f stand for pressure, velocity and the bulk modulus of the fluid, respectively.

$$\begin{cases} -p^t = \sigma_{zz}^b - \phi^b p^b \\ \sigma_{zx}^t = 0 \\ p^t = p^b \\ \dot{U}_z^t = (1 - \phi^b) \dot{u}_z^b + \phi^b \dot{U}_z^b \end{cases} \quad (C3)$$

The equations with corresponding constitutive relations are (Wu *et al.* 1990)

$$\begin{cases} \kappa_f^t (\nabla \cdot U^t) = (P^b - 2N^b + Q^b) \frac{\partial u_x^b}{\partial x} + (P^b + Q^b) \frac{\partial u_z^b}{\partial z} + (Q^b + R^b)(\nabla \cdot U^b) \\ 0 = \left(\frac{\partial u_z^t}{\partial x} + \frac{\partial u_x^t}{\partial z} \right) \\ \kappa_f^t (\nabla \cdot U^t) = (Q^b (\nabla \cdot u^b) + R^b (\nabla \cdot U^b)) / \phi^b \\ \dot{U}_z^t = \phi^b \dot{U}_z^b + (1 - \phi^b) \dot{u}_z^b. \end{cases} \quad (C4)$$

APPENDIX D: DERIVATION OF THE PLANE-WAVE ANALYSIS

Here we derive the plane-wave analysis for the three interface conditions.

D1 Poroelastic/poroelastic interface

For the poreporoelastic/poroelastic interface, the x and z components of displacement of waves propagating in the top and the bottom poroelastic media are

$$\begin{cases} u'_x = \frac{\partial \phi'_+}{\partial x} + \frac{\partial \phi'_-}{\partial x} - \frac{\partial \psi^t}{\partial z} = ik_x(1 + B'_+) + ik_x B'_- - i\gamma'_{sh} C^t \\ u'_z = \frac{\partial \phi'_+}{\partial z} + \frac{\partial \phi'_-}{\partial z} + \frac{\partial \psi^t}{\partial x} = -i\gamma'_+ + i\gamma'_+ B'_+ + i\gamma'_- B'_- + ik_x C^t \\ u^b_x = \frac{\partial \phi^b_+}{\partial x} + \frac{\partial \phi^b_-}{\partial x} - \frac{\partial \psi^b}{\partial z} = ik_x B^b_+ + ik_x B^b_- + i\gamma^b_{sh} C^b \\ u^b_z = \frac{\partial \phi^b_+}{\partial z} + \frac{\partial \phi^b_-}{\partial z} + \frac{\partial \psi^b}{\partial x} = -i\gamma^b_+ B^b_+ - i\gamma^b_- B^b_- + ik_x C^b. \end{cases} \tag{D1}$$

Their derivatives of with respect to x and z are

$$\begin{cases} \frac{\partial u^t_x}{\partial x} = \frac{\partial^2 \phi'_+}{\partial x^2} + \frac{\partial^2 \phi'_-}{\partial x^2} - \frac{\partial^2 \psi^t}{\partial z^2} = -k_x^2(1 + B'_+) - k_x^2 B'_- + \gamma'_{sh} k_x C^t \\ \frac{\partial u^t_x}{\partial z} = \frac{\partial^2 \phi'_+}{\partial x \partial z} + \frac{\partial^2 \phi'_-}{\partial x \partial z} + \frac{\partial^2 \psi^t}{\partial z^2} = k_x \gamma'_+(1 - B'_+) + k_x \gamma'_- B'_- + (\gamma'_{sh})^2 C^t \\ \frac{\partial u^t_z}{\partial x} = \frac{\partial^2 \phi'_+}{\partial z \partial x} + \frac{\partial^2 \phi'_-}{\partial z \partial x} - \frac{\partial^2 \psi^t}{\partial x^2} = k_x \gamma'_+(1 - B'_+) - k_x \gamma'_- B'_- - k_x^2 C^t \\ \frac{\partial u^t_z}{\partial z} = \frac{\partial^2 \phi'_+}{\partial z^2} + \frac{\partial^2 \phi'_-}{\partial z^2} + \frac{\partial^2 \psi^t}{\partial x \partial z} = -(\gamma'_+)^2(1 + B'_+) - (\gamma'_-)^2 B'_- - k_x \gamma'_{sh} C^t \\ \frac{\partial u^b_x}{\partial x} = \frac{\partial^2 \phi^b_+}{\partial x^2} + \frac{\partial^2 \phi^b_-}{\partial x^2} - \frac{\partial^2 \psi^b}{\partial z^2} = -k_x^2 B^b_+ - k_x^2 B^b_- - \gamma^b_{sh} k_x C^b \\ \frac{\partial u^b_x}{\partial z} = \frac{\partial^2 \phi^b_+}{\partial x \partial z} + \frac{\partial^2 \phi^b_-}{\partial x \partial z} + \frac{\partial^2 \psi^b}{\partial z^2} = k_x \gamma^b_+ B^b_+ + k_x \gamma^b_- B^b_- + (\gamma^b_{sh})^2 C^b \\ \frac{\partial u^b_z}{\partial x} = \frac{\partial^2 \phi^b_+}{\partial z \partial x} + \frac{\partial^2 \phi^b_-}{\partial z \partial x} - \frac{\partial^2 \psi^b}{\partial x^2} = k_x \gamma^b_+ B^b_+ + k_x \gamma^b_- B^b_- - k_x^2 C^b \\ \frac{\partial u^b_z}{\partial z} = \frac{\partial^2 \phi^b_+}{\partial z^2} + \frac{\partial^2 \phi^b_-}{\partial z^2} + \frac{\partial^2 \psi^b}{\partial x \partial z} = -(\gamma^b_+)^2 B^b_+ - (\gamma^b_-)^2 B^b_- + k_x \gamma^b_{sh} C^b. \end{cases} \tag{D2}$$

The x and z components of displacement of waves propagating in the fluid parts of the poroelastic media are

$$\begin{cases} U^t_x = -\varrho'_+ \frac{\partial \phi'_+}{\partial x} - \varrho'_- \frac{\partial \phi'_-}{\partial x} - \varrho'_{sh} \frac{\partial \psi^t}{\partial z} = -i\varrho'_+ k_x(1 + B'_+) - i\varrho'_- k_x B'_- - i\varrho'_{sh} \gamma'_{sh} C^t \\ U^t_z = -\varrho'_+ \frac{\partial \phi'_+}{\partial z} - \varrho'_- \frac{\partial \phi'_-}{\partial z} + \varrho'_{sh} \frac{\partial \psi^t}{\partial x} = -i\varrho'_+ \gamma'_+(-1 + B'_+) - i\varrho'_- \gamma'_- B'_- + i\varrho'_{sh} k_x C^t \\ U^b_x = -\varrho^b_+ \frac{\partial \phi^b_+}{\partial x} - \varrho^b_- \frac{\partial \phi^b_-}{\partial x} - \varrho^b_{sh} \frac{\partial \psi^b}{\partial z} = -i\varrho^b_+ k_x B^b_+ - i\varrho^b_- k_x B^b_- + i\varrho^b_{sh} \gamma^b_{sh} C^b \\ U^b_z = -\varrho^b_+ \frac{\partial \phi^b_+}{\partial z} - \varrho^b_- \frac{\partial \phi^b_-}{\partial z} + \varrho^b_{sh} \frac{\partial \psi^b}{\partial x} = i\varrho^b_+ \gamma^b_+ B^b_+ + i\varrho^b_- \gamma^b_- B^b_- + i\varrho^b_{sh} k_x C^b. \end{cases} \tag{D3}$$

Their derivatives of with respect to x and z are

$$\begin{cases} \frac{\partial U^t_x}{\partial x} = -\varrho'_+ \frac{\partial^2 \phi'_+}{\partial x^2} - \varrho'_- \frac{\partial^2 \phi'_-}{\partial x^2} - \varrho'_{sh} \frac{\partial^2 \psi^t}{\partial x \partial z} = \varrho'^t k_x^2(1 + B'_+) + \varrho'^t k_x^2 B'_- + \varrho'_{sh} \gamma'_{sh} k_x C^t \\ \frac{\partial U^t_z}{\partial z} = -\varrho'_+ \frac{\partial^2 \phi'_+}{\partial z^2} - \varrho'_- \frac{\partial^2 \phi'_-}{\partial z^2} - \varrho'_{sh} \frac{\partial^2 \psi^t}{\partial x \partial z} = \varrho'^t (\gamma'_+)^2(1 + B'_+) + \varrho'^t (\gamma'_-)^2 B'_- - \varrho'_{sh} k_x \gamma'_{sh} C^t \\ \frac{\partial U^b_x}{\partial x} = -\varrho^b_+ \frac{\partial^2 \phi^b_+}{\partial x^2} - \varrho^b_- \frac{\partial^2 \phi^b_-}{\partial x^2} - \varrho^b_{sh} \frac{\partial^2 \psi^b}{\partial x \partial z} = \varrho^b_+ k_x^2 B^b_+ + \varrho^b_- k_x^2 B^b_- - \varrho^b_{sh} \gamma^b_{sh} k_x C^b \\ \frac{\partial U^b_z}{\partial z} = -\varrho^b_+ \frac{\partial^2 \phi^b_+}{\partial z^2} - \varrho^b_- \frac{\partial^2 \phi^b_-}{\partial z^2} - \varrho^b_{sh} \frac{\partial^2 \psi^b}{\partial x \partial z} = \varrho^b_+ (\gamma^b_+)^2 B^b_+ + \varrho^b_- (\gamma^b_-)^2 B^b_- + \varrho^b_{sh} k_x \gamma^b_{sh} C^b. \end{cases} \tag{D4}$$

Inserting the above equations into the corresponding 6 equations of the poroelastic/poroelastic interface condition yields the linear system of eq. (12) after simplifying, where the elements of the 6×6 Matrix W are:

$$W = \begin{pmatrix} w_{11} & w_{12} & -2N^t k_x \gamma_{sh} & w_{14} & w_{14} & -2N^b k_x \gamma^b_{sh} \\ 2N^t k_x \gamma'_+ & 2N^t k_x \gamma'_- & 2N^t [k_x^2 - (\gamma'_+)^2] & 2N^b k_x \gamma^b_+ & 2N^b k_x \gamma^b_- & 2N^b [(\gamma^b_+)^2 - k_x^2] \\ w_{31} & w_{32} & 0 & w_{34} & w_{35} & 0 \\ \gamma'_+ & \gamma'_- & k_x & \gamma^b_+ & \gamma^b_- & -k_x \\ k_x & k_x & -\gamma'_{sh} & -k_x & -k_x & -\gamma^b_{sh} \\ w_{61} & w_{62} & \phi^t k_x (1 - \varrho'_{sh}) & w_{64} & w_{65} & \phi^b k_x (\varrho^b_{sh} - 1), \end{pmatrix} \tag{D5}$$

where w_{13} and w_{14} are given by

$$\begin{cases} w_{11} = -(P^t - 2N^t + Q^t)k_x^2 - (P^t + Q^t)(\gamma_+^t)^2 + (Q^t + R^t)\varrho_+^t[k_x^2 + (\gamma_+^t)^2] \\ w_{12} = -(P^t - 2N^t + Q^t)k_x^2 - (P^t + Q^t)(\gamma_-^t)^2 + (Q^t + R^t)\varrho_-^t[k_x^2 + (\gamma_-^t)^2] \\ w_{14} = (P^b - 2N^b + Q^b)k_x^2 - (P^b + Q^b)(\gamma_+^b)^2 + (Q^b + R^b)\varrho_+^b[k_x^2 + (\gamma_+^b)^2] \\ w_{15} = (P^b - 2N^b + Q^b)k_x^2 - (P^b + Q^b)(\gamma_-^b)^2 + (Q^b + R^b)\varrho_-^b[k_x^2 + (\gamma_-^b)^2] \\ w_{31} = -1/\phi^t Q^t[k_x^2 + (\gamma_+^t)^2] + 1/\phi^t R^t \varrho_+^t[k_x^2 + (\gamma_+^t)^2] \\ w_{32} = -1/\phi^t Q^t[k_x^2 + (\gamma_-^t)^2] + 1/\phi^t R^t \varrho_-^t[k_x^2 + (\gamma_-^t)^2] \\ w_{34} = 1/\phi^b Q^b[k_x^2 + (\gamma_+^b)^2] - 1/\phi^b R^b \varrho_+^b[k_x^2 + (\gamma_+^b)^2] \\ w_{35} = 1/\phi^b Q^b[k_x^2 + (\gamma_-^b)^2] - 1/\phi^b R^b \varrho_-^b[k_x^2 + (\gamma_-^b)^2] \\ w_{61} = \phi^t \gamma_+^t (1 + \varrho_+^t) \\ w_{62} = \phi^t \gamma_-^t (1 + \varrho_-^t) \\ w_{64} = \phi^b \gamma_+^b (1 + \varrho_+^b) \\ w_{65} = \phi^b \gamma_-^b (1 + \varrho_-^b). \end{cases} \tag{D6}$$

The elements of 6×1 vector \mathbf{Z} is as follows:

$$\mathbf{Z} = [z_1, 2N^t k_x \gamma_+^t, z_3, \gamma_+^t, -k_x, z_6]^T, \tag{D7}$$

where $z_1, z_3,$ and z_6 are given by

$$\begin{cases} z_1 = (P^t - 2N^t + Q^t)k_x^2 + (P^t + Q^t)(\gamma_+^t)^2 - (Q^t + R^t)\varrho_+^t[k_x^2 + (\gamma_+^t)^2] \\ z_3 = 1/\phi^t Q^t[k_x^2 + (\gamma_+^t)^2] - 1/\phi^t R^t \varrho_+^t[k_x^2 + (\gamma_+^t)^2] \\ z_6 = \phi^t \gamma_+^t (1 + \varrho_+^t) \end{cases} \tag{D8}$$

The R/T coefficients of the potential functions $B_+^t, B_-^t, C^t, B_+^b, B_-^b, C^b$ can be obtained by solving the linear system, which are further used to calculate the R/T coefficients of displacements with eq. (D1) for the reflected fast P , slow P and S waves in the top poroelastic medium and equations for the transmitted fast P , slow and S waves in the bottom poroelastic medium (D3), respectively.

D2 Elastic/poroelastic interface

For the elastic/poroelastic interface, we use γ^t, ϕ^t and B^t to denote the vertical component of the P wave vector, P wave potential and its reflection coefficient in the top elastic medium. The x and z components of displacement of waves propagating in the top elastic medium are

$$\begin{cases} u_x^t = \frac{\partial \phi^t}{\partial x} - \frac{\partial \psi^t}{\partial z} = ik_x(1 + B^t) - i\gamma_{sh}^t C^t \\ u_z^t = \frac{\partial \phi^t}{\partial z} + \frac{\partial \psi^t}{\partial x} = i\gamma^t(-1 + B^t) + ik_x C^t. \end{cases} \tag{D9}$$

Their derivatives of with respect to x and z are

$$\begin{cases} \frac{\partial u_x^t}{\partial x} = \frac{\partial^2 \phi^t}{\partial x^2} - \frac{\partial^2 \psi^t}{\partial x \partial z} = -k_x^2(1 + B^t) + \gamma_{sh}^t k_x C^t \\ \frac{\partial u_x^t}{\partial z} = \frac{\partial \phi^t}{\partial x \partial z} - \frac{\partial^2 \psi^t}{\partial z^2} = k_x \gamma^t(1 - B^t) + (\gamma_{sh}^t)^2 C^t \\ \frac{\partial u_z^t}{\partial x} = \frac{\partial^2 \phi^t}{\partial z \partial x} + \frac{\partial^2 \psi^t}{\partial x^2} = k_x \gamma^t(1 - B^t) - k_x^2 C^t \\ \frac{\partial u_z^t}{\partial z} = \frac{\partial^2 \phi^t}{\partial z^2} + \frac{\partial^2 \psi^t}{\partial x \partial z} = -(\gamma^t)^2(1 + B^t) - k_x \gamma_{sh}^t C^t. \end{cases} \tag{D10}$$

Inserting the above equations into the corresponding five equations of the elastic/poroelastic interface condition (C2) yields a linear system, where the elements of the 5×5 Matrix \mathbf{W} are:

$$\mathbf{W} = \begin{pmatrix} w_{11} & 2N^t \gamma_{sh}^t k_x & w_{13} & w_{14} & 2N^b \gamma_{sh}^b k_x \\ 2N^t k_x \gamma^t & 2N^t [k_x^2 - (\gamma_{sh}^t)^2] & 2N^b (\gamma_+^b k_x) & 2N^b (\gamma_-^b k_x) & N^b [(\gamma_{sh}^b)^2 - k_x^2] \\ \gamma^t & k_x & \gamma_+^b & \gamma_-^b & -k_x \\ k_x & -\gamma_{sh}^t & -k_x & -k_x & -\gamma_{sh}^b \\ 0 & 0 & (\varrho_+^b + 1)\gamma_+^b & (\varrho_-^b + 1)\gamma_-^b & (\varrho_{sh}^b - 1)k_x \end{pmatrix}, \tag{D11}$$

where w_{13} and w_{14} are given by

$$\begin{cases} w_{11} = (P^t - 2N^t)k_x^2 + P^t(\gamma^t)^2 \\ w_{13} = -(P^b - 2N^b + Q^b)k_x^2 - (P^b + Q^b)(\gamma_+^b)^2 + (Q^b + R^b)\varrho_+^b[k_x^2 + (\gamma_+^b)^2] \\ w_{14} = -(P^b - 2N^b + Q^b)k_x^2 - (P^b + Q^b)(\gamma_-^b)^2 + (Q^b + R^b)\varrho_-^b[k_x^2 + (\gamma_-^b)^2]. \end{cases} \quad (\text{D12})$$

The elements of 5×1 vector \mathbf{Z} is as follows:

$$\mathbf{Z} = [-(P^t - 2N^t)k_x^2 - P^t(\gamma^t)^2, 2N^t k_x \gamma^t, \gamma^t, -k_x, 0]^T. \quad (\text{D13})$$

The R/T coefficients of the potential functions $B^t, C^t, B_+^b, B_-^b, C^b$ can be obtained by solving the linear system, which are further used to calculate the R/T coefficients of displacements with eq. (D9) for the reflected P and S waves in the elastic medium and equations for the transmitted fast P and S waves in the poroelastic medium (D3), respectively.

D3 Acoustic/poroelastic interface

For the acoustic/poroelastic interface, we use γ_p^t, ϕ^t and B^t to denote the vertical component of the P wave vector, P wave potential and its reflection coefficient in the top elastic medium. The x and z components of displacement of waves propagating in the top acoustic medium are

$$\begin{cases} U_x^t = \frac{\partial \phi^t}{\partial x} = ik_x(1 + B^t) \\ U_z^t = \frac{\partial \phi^t}{\partial z} = i\gamma_p^t(-1 + B^t). \end{cases} \quad (\text{D14})$$

Their derivatives of with respect to x and z are

$$\begin{cases} \frac{\partial u_x^t}{\partial x} = \frac{\partial^2 \phi^t}{\partial x^2} = -k_x^2(1 + B^t) \\ \frac{\partial u_x^t}{\partial z} = \frac{\partial \phi^t}{\partial x \partial z} = k_x \gamma_p^t(1 - B^t) \\ \frac{\partial u_z^t}{\partial x} = \frac{\partial^2 \phi^t}{\partial z \partial x} = k_x \gamma_p^t(1 - B^t) \\ \frac{\partial u_z^t}{\partial z} = \frac{\partial^2 \phi^t}{\partial z^2} = -(\gamma_p^t)^2(1 + B^t). \end{cases} \quad (\text{D15})$$

Inserting the above equations into the corresponding four equations of the acoustic/poroelastic interface condition (C4) yields a linear system of equations, where the elements of the 4×4 Matrix \mathbf{W} are:

$$\mathbf{W} = \begin{pmatrix} -\rho\omega^2 & w_{12} & w_{13} & -2N^b \gamma_{sh}^b k_x \\ 0 & 2N^b [k_x^2 - (\gamma_+^b)^2] & 2N^b (\gamma_-^b k_x) & (\gamma_{sh}^b)^2 - k_x^2 \\ \gamma_p^t & -\varrho_+^b \phi^b \gamma_+^b & -\varrho_-^b \phi^b \gamma_-^b & \varrho_{sh}^b \phi^b k_x \\ \rho & w_{42} & w_{43} & 0 \end{pmatrix}. \quad (\text{D16})$$

where ρ is the density of the acoustic medium. w_{13} and w_{14} are given by

$$\begin{cases} w_{12} = (P^b - 2N^b + Q^b)k_x^2 + (P^b + Q^b)(\gamma_+^b)^2 - (Q^b + R^b)\varrho_+^b[k_x^2 + (\gamma_+^b)^2] \\ w_{13} = (P^b - 2N^b + Q^b)k_x^2 + (P^b + Q^b)(\gamma_-^b)^2 - (Q^b + R^b)\varrho_-^b[k_x^2 + (\gamma_-^b)^2] \\ w_{42} = 1/\phi^b (R^b \varrho_+^b - Q^b)[k_x^2 + (\gamma_p^b)^2] \\ w_{43} = 1/\phi^b (R^b \varrho_-^b - Q^b)[k_x^2 + (\gamma_p^b)^2]. \end{cases} \quad (\text{D17})$$

The elements of 4×1 vector \mathbf{Z} is as follows:

$$\mathbf{Z} = [\rho\omega^2, 0, \gamma_p^t, -\rho]^T. \quad (\text{D18})$$

The R/T coefficients of the potential functions B^t, B_+^b, B_-^b, C^b can be obtained by solving the linear system, which are further used to calculate the R/T coefficients of displacements with eq. (D14) for the reflected P wave in the top acoustic medium and equations for the transmitted fast P and S waves in the poroelastic medium (D3), respectively.